Matter

Synthesis of high-quality large $Cr_2TiC_2T_x$ MXene monolayers, their mechanical properties, *p*-type electrical transport, and positive photoresponse

Graphical abstract

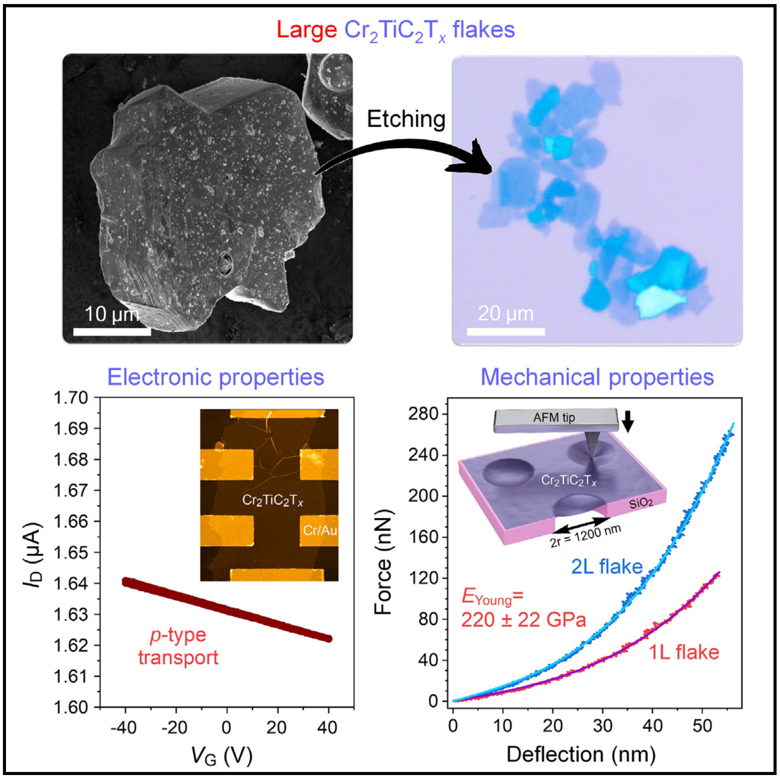

Highlights

- A method for large high-quality flakes of $Cr_2TiC_2T_x$ MXene is presented
- $Cr_2TiC_2T_x$ single-flake devices show *p*-type transport and positive photoresponse
- $Cr_2TiC_2T_x$ flakes exhibit effective Young's modulus of 220 ± 22 GPa
- DFT suggests $Cr_2TiC_2T_x$ may have tunable structure-dependent *p*-/*n*-type properties

Benchmark

First qualification/assessment of material properties and/or performance

Authors

Saman Bagheri, Michael J. Loes, Alexey Lipatov, ..., Md. Ibrahim Kholil, Alexei Gruverman, Alexander Sinitskii

Correspondence

sinitskii@unl.edu

In brief

We report synthesis of high-quality $Cr_2TiC_2T_x$ monolayers with lateral sizes exceeding 15 μm for single-flake measurements. These measurements establish $Cr_2TiC_2T_x$ as a unique material among the MXenes experimentally tested so far. Field-effect electrical measurements on $Cr_2TiC_2T_x$ monolayers revealed their *p*-type transport and positive photoresponse, while $Ti_3C_2T_x$, the most established MXene, has *n*-type behavior and negative photoresponse. Nanoindentation measurements of monolayer $Cr_2TiC_2T_x$ membranes yielded an effective Young's modulus of 220 ± 22 GPa. Density functional theory calculations suggest that $Cr_2TiC_2T_x$ may have tunable structure-dependent *p*-/*n*-type properties.

Bagheri et al., 2024, Matter *7*, 1–16
December 4, 2024
https://doi.org/10.1016/j.matt.2024.08.019

CellPress

Please cite this article in press as: Bagheri et al., Synthesis of high-quality large $Cr_2TiC_2T_x$ MXene monolayers, their mechanical properties, *p*-type electrical transport, and positive photoresponse, MATT (2024), https://doi.org/10.1016/j.matt.2024.08.019

Matter

CellPress

Article

Synthesis of high-quality large $Cr_2TiC_2T_x$ MXene monolayers, their mechanical properties, *p*-type electrical transport, and positive photoresponse

Saman Bagheri,[1] Michael J. Loes,[1] Alexey Lipatov,[1,2] Khimananda Acharya,[3] Tula R. Paudel,[3] Haidong Lu,[4] Rashmeet Khurana,[1] Md. Ibrahim Kholil,[1] Alexei Gruverman,[4,5] and Alexander Sinitskii[1,5,6,*]

[1]Department of Chemistry, University of Nebraska-Lincoln, Lincoln, NE 68588, USA
[2]Department of Chemistry, Biology, and Health Sciences, South Dakota School of Mines and Technology, Rapid City, SD 57701, USA
[3]Department of Physics, South Dakota School of Mines and Technology, Rapid City, SD 57701, USA
[4]Department of Physics and Astronomy, University of Nebraska-Lincoln, Lincoln, NE 68588, USA
[5]Nebraska Center for Materials and Nanoscience, University of Nebraska-Lincoln, Lincoln, NE 68588, USA
[6]Lead contact
*Correspondence: sinitskii@unl.edu
https://doi.org/10.1016/j.matt.2024.08.019

PROGRESS AND POTENTIAL This work provides access to large high-quality flakes of $Cr_2TiC_2T_x$ MXene, which has been shown to have a unique combination of physical properties. The described multifaceted synthetic approach focusing on the quality and purity of the precursor Cr_2TiAlC_2 MAX phase, the size distribution of MAX phase particles, and the efficiency of the etching, intercalation, and delamination procedures, is likely applicable to the optimization of syntheses of other MXene materials, especially those for which large high-quality monolayers are currently not available. Because of its attractive mechanical and transport characteristics that are complementary to other established MXenes, $Cr_2TiC_2T_x$ can find applications on its own as well as in combination with other MXene materials. For example, the composites and layered heterostructures that make up *p*-type $Cr_2TiC_2T_x$ and *n*-type MXenes, such as $Ti_3C_2T_x$, may present tunable electronic and optoelectronic characteristics.

SUMMARY

$Cr_2TiC_2T_x$ is an ordered double-transition-metal MXene with peculiar magnetic properties. Previous studies produced sub-1-μm sheets of $Cr_2TiC_2T_x$, which prevented complete characterization of its intrinsic properties at a single-flake level. We report the synthesis of high-quality $Cr_2TiC_2T_x$ monolayers with lateral sizes exceeding 15 μm for single-flake measurements. These measurements establish $Cr_2TiC_2T_x$ as a unique material among the MXenes experimentally tested so far. Field-effect electrical measurements on $Cr_2TiC_2T_x$ monolayers revealed an average conductivity of 180 S cm^{-1} and *p*-type transport, while established MXenes, such as $Ti_3C_2T_x$ and $Nb_4C_3T_x$, demonstrated *n*-type behavior. In contrast to negative photoresponse reported for $Ti_3C_2T_x$ flakes, $Cr_2TiC_2T_x$ devices show positive photoresponse to visible and infrared light. Nanoindentation measurements of monolayer $Cr_2TiC_2T_x$ membranes yielded an effective Young's modulus of 220 ± 22 GPa. Density functional theory calculations provide insights into the *p*-type character of $Cr_2TiC_2T_x$ and predict its potentially tunable *p*-/*n*-type behavior depending on the concentrations of Cr vacancies, oxygens substituting carbon atoms, and surface terminations.

INTRODUCTION

MXenes are a class of two-dimensional (2D) materials with a general formula of $M_{n+1}X_nT_x$, where M is a transition metal, X is C or N, and T_x corresponds to surface functional groups.[1,2] The chemical and structural diversity of MXenes, as well as their scalability and processability, are the reasons for their thriving in many applications.[1,2] However, while over 30 MXenes based on different combinations of M and X elements have been synthesized and many others theoretically predicted, most experimental research so far has been focused on $Ti_3C_2T_x$,[1] which is the first reported MXene material.[3] Much fewer studies have been focused on other single-transition metal MXenes, such as Ti_2CT_x,[4,5] Nb_2CT_x,[6–8] Ti_3CNT_x,[4,7,9] V_2CT_x,[8,10,11] $Nb_4C_3T_x$,[7,12–14] and $Ta_4C_3T_x$,[4,15] and, compared to $Ti_3C_2T_x$, little is known about the properties of multielement MXenes, such as $TiVNbMoC_3T_x$,[16]

Please cite this article in press as: Bagheri et al., Synthesis of high-quality large $Cr_2TiC_2T_x$ MXene monolayers, their mechanical properties, *p*-type electrical transport, and positive photoresponse, MATT (2024), https://doi.org/10.1016/j.matt.2024.08.019

$Mo_2TiC_2T_x$,[17] $(V_{0.5},Cr_{0.5})_3C_2T_x$,[4] and $Cr_2TiC_2T_x$.[18] However, there are already promising indications that these less studied materials offer many intriguing properties that are not available in their more established MXene counterparts. For example, $Cr_2TiC_2T_x$, a recently synthesized ordered double-transition-metal MXene, was shown to have a peculiar magnetic transition around 30 K in bulk films,[18] which distinguishes it from $Ti_3C_2T_x$ and other MXenes without known magnetic properties.

One important obstacle preventing the characterization of intrinsic properties of emerging MXenes is the lack of synthetic procedures enabling preparation of these materials in a form of large monolayers that are suitable for single-flake electrical and mechanical property measurements. Unlike graphene and transition metal chalcogenides, which can be grown on a wafer scale by chemical vapor deposition,[19,20] the synthesis of MXenes commonly involves chemical etching of the precursor MAX phase particles in a solution.[1,2] The resulting flakes may contain a high level of defects and are often less than 1 μm in size.[10,11,21–23] At the same time, large uniform flakes, when available, open numerous opportunities for research and applications of MXenes in many areas, such as high-voltage interconnects, electronic devices, and resonators.[13,24,25] Over the last decade, there has been significant improvement in the quality of $Ti_3C_2T_x$ MXene, which evolved from small and highly defective flakes synthesized using hydrofluoric acid (HF) and a sonication-assisted method[26] to relatively large (~10 μm) flakes, with a minimum level of defects prepared via the minimally intensive layer delamination method[26,27] to the very uniform flakes with lateral sizes >40 μm produced by the soft delamination method.[28] Intrinsic physical properties of high-quality few-micrometer flakes can be probed by the lithographic fabrication of nanoscale devices for electrical characterization[9,13,14,25,27,29] or suspended membranes for nanoindentation-based mechanical measurements.[13,30] In the case of $Ti_3C_2T_x$ MXene, such measurements revealed a number of very attractive properties, such as high electrical conductivities of up to 11,000 S cm^{-1}, high breakdown current densities of about 1.2×10^8 A cm^{-2}, and a high effective Young's modulus of about 330 GPa.[25,30]

$Cr_2TiC_2T_x$ is one of many MXenes that have not been tested on a single-flake level yet despite its intriguing physical properties demonstrated in bulk measurements.[18] The original report on the synthesis of $Cr_2TiC_2T_x$ demonstrated sub-1-μm flakes[18] that were too small for multielectrode device patterning or fabrication of suspended membranes. In this study, we report the improved synthesis of bulk quantities of large (>10 μm) 2D sheets of $Cr_2TiC_2T_x$. Few-micrometer flakes without microscopically visible holes, tears, degradation, or contamination were used for mechanical, electronic, and optoelectronic measurements. We studied various factors that directly affect the synthesis yield and the quality of the prepared MXene, including the fabrication of the MAX phase, optimization of the etching and intercalation processes, and centrifugation-assisted delamination. Results show an improvement over the previous report and a successful synthesis of high-quality $Cr_2TiC_2T_x$ flakes with lateral sizes >15 μm and reduced levels of defects.

The results of single-flake measurements on $Cr_2TiC_2T_x$ further establish it as a unique material among MXenes experimentally tested so far. We fabricated field-effect transistor (FET) devices based on individual monolayer $Cr_2TiC_2T_x$ flakes and tested their electronic and optoelectronic properties. Based on the results of field-effect electrical measurements, $Cr_2TiC_2T_x$ is shown to be the first MXene with a *p*-type transport, while other MXene materials tested on a single-flake level, such as $Ti_3C_2T_x$ and $Nb_4C_3T_x$, demonstrated *n*-type behavior in similar measurements.[13,25,29] The *p*-type character of $Cr_2TiC_2T_x$ is shown to be consistent with the results of density functional theory (DFT) calculations. We also tested the photocurrent in $Cr_2TiC_2T_x$ devices when they were illuminated with either white light or different lasers in the visible or infrared range of the spectrum. Recently, such measurements were performed on monolayer $Ti_3C_2T_x$ MXene, and Vorobeva et al. demonstrated that it exhibits a negative photoresponse, such that the device current decreases under illumination.[27] In contrast to the prototypical $Ti_3C_2T_x$ MXene, $Cr_2TiC_2T_x$ demonstrates a positive photoresponse, with the current increasing under illumination. We also fabricated high-quality membranes based on monolayer and bilayer $Cr_2TiC_2T_x$ flakes suspended over circular microwells. The nanoindentation measurements performed on these membranes using atomic force microscopy (AFM) revealed the effective Young's modulus of 220 ± 22 GPa. While lower than determined for $Ti_3C_2T_x$ and $Nb_4C_3T_x$ in similar nanoindentation experiments,[13,30] this is still a respectable value within the broad family of 2D materials, suggesting the potential use of $Cr_2TiC_2T_x$ for a variety of mechanical applications. Furthermore, since many of the characteristics of $Cr_2TiC_2T_x$ appear to be complementary to the properties of other more established MXenes, notably $Ti_3C_2T_x$, this work opens opportunities for materials design by combining different MXene materials in various composites and layered heterostructures.

RESULTS AND DISCUSSION

Synthesis of large high-quality flakes of $Cr_2TiC_2T_x$ MXene

Comparison of synthetic methods

The synthesis of large high-quality flakes of MXenes is very important for device fabrication.[14,24,28,29] A typical synthesis of MXenes involves the use of an HF-based etchant, intercalation of multilayer (ML) MXene with tetramethylammonium hydroxide (TMAOH), and a long sonication, which results in mainly submicrometer flakes with a high level of defects.[26] The first reported synthesis of $Cr_2TiC_2T_x$ flakes[18] was not an exception and followed a similar process utilizing HF-based etchant and sonication. As a result, the flakes produced by this approach suffer from structural degradation, such as visible holes and tears, that are expected to adversely affect MXene properties, such as electrical conductivity, charge carrier mobility, and mechanical and structural stability. We reproduced the HF-based synthesis of $Cr_2TiC_2T_x$ reported earlier[18] and studied the microstructure of the produced flakes. The synthesis process involves etching of the Cr_2TiAlC_2 MAX phase using a mixture of HF and HCl, followed by overnight intercalation with TMAOH and sonication for 30 min. The $Cr_2TiC_2T_x$ flakes produced in this process are often <1 μm and contain structural defects, as seen in the transmission electron microscopy (TEM) images in Figure 1A. The high-resolution TEM (HRTEM) characterization of this MXene reveals the

Please cite this article in press as: Bagheri et al., Synthesis of high-quality large $Cr_2TiC_2T_x$ MXene monolayers, their mechanical properties, *p*-type electrical transport, and positive photoresponse, MATT (2024), https://doi.org/10.1016/j.matt.2024.08.019

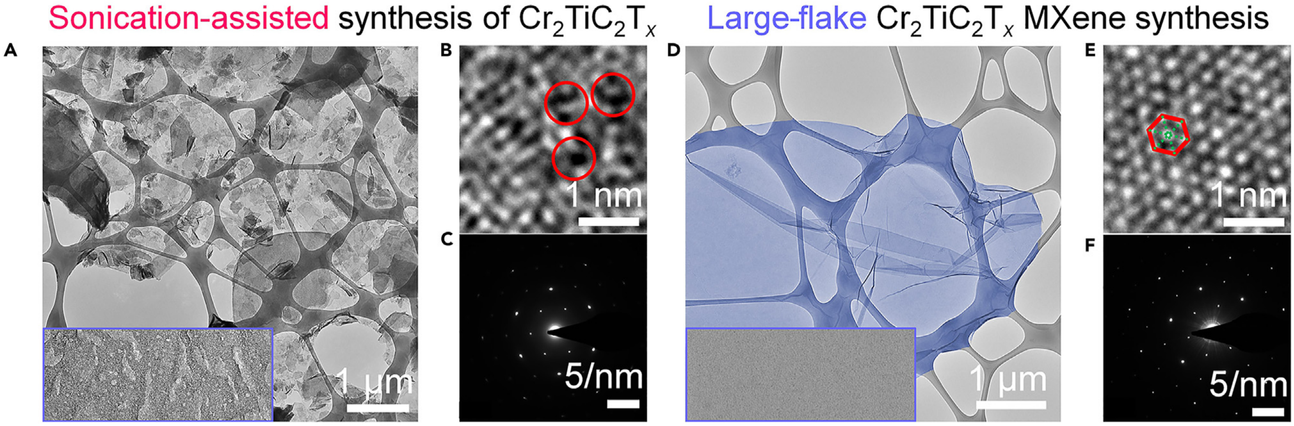

Figure 1. Electron microscopy characterization of $Cr_2TiC_2T_x$

(A) TEM image of $Cr_2TiC_2T_x$ synthesized through the conventional method. The inset shows a higher magnification of a representative MXene flake, revealing structural defects.

(B) HRTEM image of a representative MXene flake from (A). Point and cluster defects are labeled with red circles.

(C) SAED pattern of the same flake.

(D) TEM image of large $Cr_2TiC_2T_x$ synthesized through the optimized method. The inset shows a higher magnification of the same flake with no visible degradation or defects.

(E) HRTEM of the flake shown in (D), with a visible hexagonal arrangement of atoms and no point defects.

(F) SAED pattern of the same flake. More diffraction spots are observed compared to (C), indicating a higher sample crystallinity.

presence of point and cluster defects, identified with red circles in Figure 1B. The $Cr_2TiC_2T_x$ produced by this approach is still a highly crystalline material, as shown by a representative selected area electron diffraction (SAED) pattern in Figure 1C, but the microscopic data suggest that there is room for improvement in terms of the average flake size and the defect density.

With the goal of investigating the intrinsic properties of $Cr_2TiC_2T_x$, we developed a synthetic method for producing high-quality few-micrometer flakes. Electron microscopy images comparing $Cr_2TiC_2T_x$ materials synthesized by different methods are summarized in Figures 1 and S1. A comparison of two TEM images in Figures 1A and 1D reveals that the optimized synthetic method yields much larger flakes with lateral dimensions of a few micrometers and no apparent defects. An HRTEM image of the same flake in Figure 1E shows no discernible point or cluster defects, and the expected hexagonal arrangement of atoms is observed. The SAED pattern in Figure 1F shows more high-order diffraction spots compared to the pattern in Figure 1C, suggesting the higher structural quality of $Cr_2TiC_2T_x$ prepared by the optimized method compared to the same MXene produced using the previously reported approach.[18] Figure S1 provides additional microscopic characterization of MXene samples prepared using the two methods. The microscopy data in Figures 1 and S1 collectively demonstrate the improvements in the flake size and structural quality of $Cr_2TiC_2T_x$ produced by the optimized procedure.

To optimize the synthetic conditions and produce high-quality large flakes, we considered the following: (1) the quality and purity of the Cr_2TiAlC_2 MAX phase, which we found to be related to the size distribution of Cr_2TiAlC_2 MAX phase particles; (2) optimization of the etching procedure; and (3) intercalation of the etched particles and their centrifugation-assisted delamination into MXene flakes.

Quality and purity of the MAX phase

The quality and purity of a MAX phase have a significant effect on the outcome of MXene synthesis,[31] making it essential to extensively characterize the precursor Cr_2TiAlC_2. First, the amount of phase impurities and their nature can adversely affect the synthesis yield, quality, and reproducibility. The more Cr- and Ti-based impurities are present in the MAX phase sample, the more etchant is consumed to remove the components that do not produce the desired $Cr_2TiC_2T_x$ product. Second, it is beneficial to have uniformly sized MAX phase particles to achieve consistent results in MXene synthesis. It is a common practice to sieve a MAX powder prior to the MXene synthesis to remove very large particles that are difficult to etch completely. We also suggest removing the smallest particles from the MAX phase powder as well, because they may only produce MXene flakes that are too small for electrical and mechanical measurements. Therefore, we used a multistep sieving approach that produces a fraction of MAX phase particles with sizes in the range of 30–40 μm, which are small enough for efficient etching and yet sufficiently large to produce MXene monolayers suitable for physical property characterization at a single-flake level.

The as-prepared Cr_2TiAlC_2 MAX phase particles have a broad size distribution, as shown in Figure S2A. Many particles are in the 100- to 150-μm range (Figure S2B), although such large particles are typically fused aggregates of smaller MAX phase crystals, as shown in Figure S2C. The as-prepared Cr_2TiAlC_2 powder was ball milled at 500 rpm for 3–5 min to crush the fused aggregates into individual crystallites. The ball-milled particles still have a broad size distribution (Figure S3A), but by sieving the powder it is possible to produce fractions of MAX phase particles that are much more uniform in size, as demonstrated by Figures S3B–S3E. The precursor Cr_2TiAlC_2 MAX phase was sieved, producing samples with particle sizes of <10 μm, 10–20 μm, 20–30 μm, and

Please cite this article in press as: Bagheri et al., Synthesis of high-quality large $Cr_2TiC_2T_x$ MXene monolayers, their mechanical properties, *p*-type electrical transport, and positive photoresponse, MATT (2024), https://doi.org/10.1016/j.matt.2024.08.019

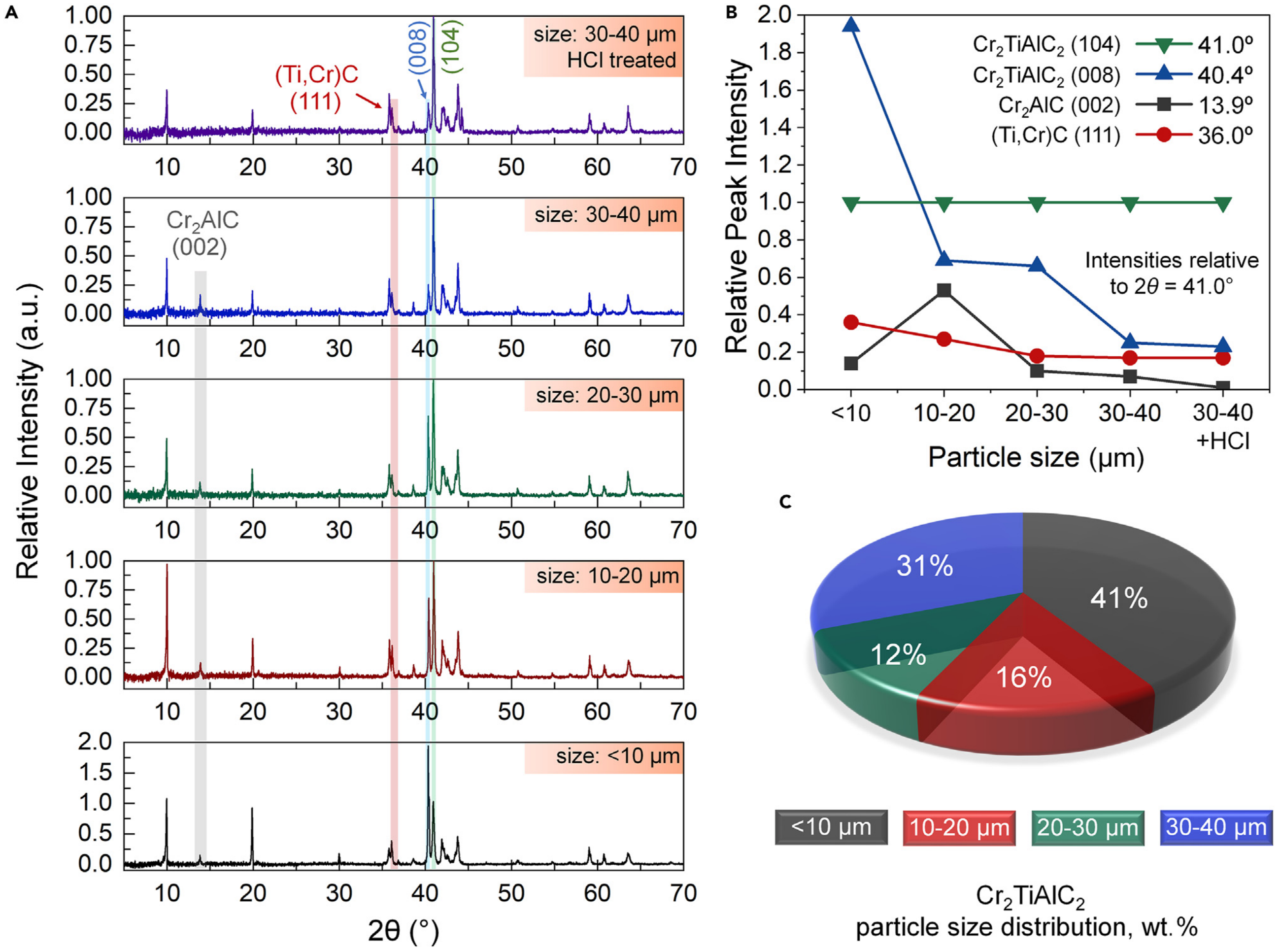

Figure 2. Powder XRD analysis of Cr_2TiAlC_2 MAX phase

(A) XRD patterns for the sieved samples, with particle size in the ranges of <10 μm, 10–20 μm, 20–30 μm, and 30–40 μm, and the HCl-treated sample with an average particle size of 30–40 μm.

(B) Relative peak ratio analysis of the major diffraction peaks at $2\theta = 13.9°$, 36.0°, 40.4°, and 41.0°, normalized based on the intensity of the $2\theta = 41.0°$ peak showing an improving trend toward a phase pure sample.

(C) Particle size distribution after ball milling and sieving of as-produced MAX phase.

30–40 μm. All samples were studied by X-ray diffraction (XRD) analysis to determine their phase composition, and the resulting powder XRD patterns are shown in Figure 2A. During the initial analysis, we identified the Cr_2AlC and (Ti,Cr)C impurity phases that are shown in Figure 2A with gray ($2\theta = 13.9°$) and red ($2\theta = 36°$) vertical bands, respectively. We believe that we have more Ti than Cr in the (Ti,Cr)C impurity phase because the cubic unit cell parameter $a = 0.43136(2)$ nm in our experiment was closer to the data in the literature for TiC ($a = 0.43247$ nm)[32] than for $Ti_{0.5}Cr_{0.5}C_{0.8}$ ($a = 0.4217$ nm).[33] We found that the amount of these impurity phases varies depending on the size of the particles. The trend is evident when we compare the peak intensities of impurities against the major (104) peak of Cr_2TiAlC_2 ($2\theta = 41.0°$). The intensity ratios of this and other major peaks at $2\theta = 13.9°$, 36.0°, and 40.4° for the MAX phase samples with different particle sizes are shown in Figure 2B. It is notable that in the sieved small-particle fractions, the intensity of the (008) peak of Cr_2TiAlC_2 at $2\theta = 40.4°$ is significantly higher than for the major (104) peak, but it drastically decreases as the particle size increases. The changes in relative intensities of the (104) and (008) peaks in Cr_2TiAlC_2 suggest highly textured grains in small particles. Furthermore, among the sieved samples, the MAX phase with the 30- to 40-μm particle sizes showed the lowest amount of (Ti,Cr)C and Cr_2AlC impurity phases.

To further improve the MAX phase quality, we treated this sample with 9 M HCl for 120 min to dissolve the Cr_2AlC residual impurities. The XRD pattern of the HCl-treated sample shown in Figure 2A (top) demonstrates the absence of the Cr_2AlC peak. Based on these results, it is recommended to not use the as-prepared Cr_2TiAlC_2 for the synthesis of $Cr_2TiC_2T_x$ but to first ball mill, sieve, and acid etch the MAX phase to obtain a relatively uniform sample that is devoid of significant impurities. Figure 2C shows the particle size distribution in the MAX powder before sieving with particles in the range of 30–40 μm, accounting for about 31 wt %.

Please cite this article in press as: Bagheri et al., Synthesis of high-quality large $Cr_2TiC_2T_x$ MXene monolayers, their mechanical properties, *p*-type electrical transport, and positive photoresponse, MATT (2024), https://doi.org/10.1016/j.matt.2024.08.019

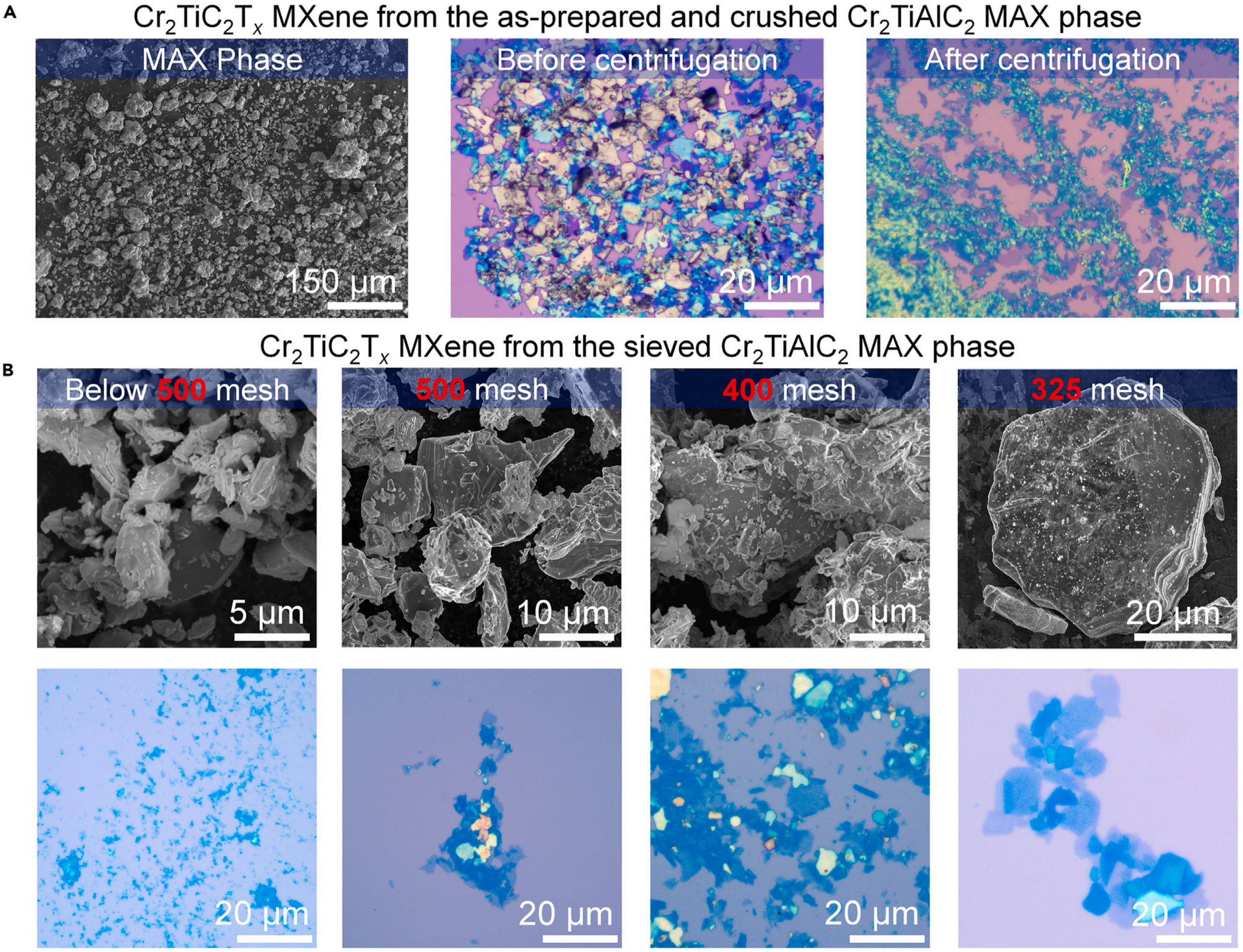

Figure 3. Electron and optical microscopy of Cr_2TiAlC_2 MAX phase samples and their corresponding $Cr_2TiC_2T_x$

(A) SEM image of the as-prepared Cr_2TiAlC_2 MAX phase and optical images of the corresponding $Cr_2TiC_2T_x$ before and after centrifugation.

(B) SEM images of the sieved Cr_2TiAlC_2 MAX phase samples and the optical images of the corresponding $Cr_2TiC_2T_x$ after centrifugation.

Etching procedure

In the MAX phase etching experiments, we tested different mixtures of diluted HF and HCl for varying periods of time. Among the conditions tested, etching 6 g of MAX phase particles for 48 h in a mixture of 18 parts HF, 32 parts HCl, and 45 parts H_2O yielded the best results in Al removal and was thus selected as optimal. Figure S4 shows scanning electron microscopy (SEM) and energy-dispersive X-ray spectroscopy (EDX) mappings of particles etched for 24 h, while Figure S5 displays SEM images of particles etched for 48 h. Synthesis times shorter than 48 h resulted in incomplete etching, as presented by the EDX mapping in Figure S4, which shows the presence of Al in the underetched MAX phase particles with incomplete layer splitting. However, a 48-h etching period, as illustrated by Figure S5, was sufficient for complete Al removal and the formation of well-split accordion-like structures. The following results represent $Cr_2TiC_2T_x$ synthesized using these optimized etching conditions.

Figure 3 illustrates the effect of sieving of the precursor MAX phase on the uniformity and quality of the MXene product. The etching of the as-prepared Cr_2TiAlC_2 samples yielded heterogeneous $Cr_2TiC_2T_x$ products in terms of the yield and flake size, so that large underetched MAX phase particles, small MXene flakes, and various intermediate structures could be simultaneously observed. An example of such a heterogeneous product produced from the as-prepared Cr_2TiAlC_2 MAX phase sample is shown in Figure 3A. Since the as-prepared MAX phase particles have a large size distribution, it is possible to simultaneously have overetched MXene flakes produced from small Cr_2TiAlC_2 particles and underetched large particles.

Etching of the processed and sieved Cr_2TiAlC_2 MAX phase samples with narrowed particle size distributions yielded more uniform $Cr_2TiC_2T_x$ products and provided additional insight into the effect of MAX phase conditioning on the outcome of MXene synthesis. Figure 3B shows sieved MAX phase crystals (SEM images) and the corresponding $Cr_2TiC_2T_x$ flakes (optical images) that were produced using the optimized synthetic conditions. Etching of MAX phase particles with sizes <10 µm was facile and had a high synthesis yield, but we mostly observed small MXene flakes in a sub-micrometer size range, which were difficult to use for device fabrication. The MXene quality improved in the case of 20- to 30-μm MAX phase particles, and it was possible to identify larger $Cr_2TiC_2T_x$ flakes in the range of 5–10 μm. The MAX phase sample with particle sizes in the range of 30–40 μm yielded the most uniform MXene product, with average flakes over 10 μm in size. The bottom right optical image in Figure 3B shows representative $Cr_2TiC_2T_x$ flakes produced from 30- to 40-μm MAX phase particles. These flakes are large, highly uniform, and could be prime candidates for device fabrication.[13,14,24,25,29,30]

It should be noted that in the previously reported method,[18] a moderate heating of 35°C was applied for the synthesis of $Cr_2TiC_2T_x$. However, even at this relatively low temperature, we observed the characteristic green color (Cr^{3+}) of the etching solution and the structural defects in HRTEM images of MXene flakes (see Figure 1B), suggesting possible acid leaching of Cr from Cr_2TiAlC_2 along with the expected removal of Al. Because of the possibility of some undesirable Cr removal from the MXene product in an HF/HCl solution, we did not heat the reaction mixture during the MAX phase etching and performed it at room temperature (~20°C).

Exfoliation of $Cr_2TiC_2T_x$ MXene flakes

For the final step, we investigated the effect of centrifugal force on the delamination of $Cr_2TiC_2T_x$ after the intercalation process (see Figure 4). After etching a MAX phase sample with particles in the range of 30–40 μm, the ML $Cr_2TiC_2T_x$ was intercalated with TMAOH for 24 h. For this process, we used 10 mL of a solution containing 2 mL 25% solution of TMAOH in methanol and 8 mL H_2O per 2 g of the initial MAX phase. We also tested lower (1 mL 25% solution of TMAOH in methanol and 9 mL H_2O per 2 g of the MAX phase) and higher (2.8 mL 25% solution of TMAOH in methanol and 7.2 mL H_2O per 2 g of the MAX phase) concentrations of TMAOH for the intercalation process. The lower concentration had a lower yield of monolayer delamination, while the higher concentration resulted in noticeably defective flakes, as shown in Figure S6.

Figure 4A contains a schematic illustration of the intercalation of ML $Cr_2TiC_2T_x$ with TMAOH, which results in the increase of the interlayer distance and expansion of the MXene stacks. The insets in Figure 4A show SEM and optical microscopy images illustrating the intercalation process. The SEM images show an increased separation of the MXene layers after the TMAOH intercalation. Furthermore, the intercalation changes the aspect ratio of the ML particles, which transform from platelets to elongated accordion-like structures. This elongation can be observed in optical photographs, as shown for a representative accordion-like structure that is marked by a blue arrow and accompanied by an illustrative scheme in the inset in Figure 4A.

It was previously demonstrated for $Ti_3C_2T_x$ that shear forces can play an important role in the effective delamination of MXene materials.[34] More specifically, the work by Zhang and coworkers notes that a centrifugation of a solution of ML $Ti_3C_2T_x$ results in the precipitation of a stable sediment, which could then be exfoliated using a vortex shaker.[34] The vortex flow of a supernatant creates a shear stress that peels the precipitated ML $Ti_3C_2T_x$ particles into monolayer flakes. We used a conceptually similar process for the exfoliation of ML $Cr_2TiC_2T_x$ MXene, although with some modifications. After the synthesis and intercalation with TMAOH, the ML $Cr_2TiC_2T_x$ was rinsed with water and centrifuged multiple times at 8,000–10,000 rpm to remove the excess TMAOH from the solution. If the centrifugation was performed using a small-volume (e.g., 50 mL) conical Falcon tube or a similar centrifuge tube, then the $Cr_2TiC_2T_x$ MXene would precipitate in a form of a compact sediment (see Figure 4B), as previously reported for $Ti_3C_2T_x$.[34] Because of the conical shape of the bottom, all MXene flakes concentrate in a small volume near the tip of a tube, where they are compacted due to the action of the centrifugal force. Optical photographs of this precipitate dispersed over a Si/SiO_2 substrate predominantly show ML MXene platelets, as demonstrated in Figure 4B (right).

Interestingly, a rheologically different product can be obtained if the centrifugation is performed in a larger (e.g., 500 mL) polypropylene centrifuge bottle with a flat bottom (as opposed to the traditional conical bottom). In this case, during the centrifugation, the ML MXene stacks do not concentrate in a small volume near the tip of a tube but instead disperse over a larger area of the flat bottom and along the walls of a bottle, resulting in their shearing and delamination. Such shearing, although implemented differently compared to the method used by Zhang et al.,[34] similarly helps in the exfoliation of MXene stacks. For optimal exfoliation, the polypropylene bottle should be filled with a MXene suspension up to ~80% by volume and centrifuged at 8,000–10,000 rpm. Lower volumes of MXene suspensions result in less effective delamination (see the scheme in Figure S7), as a smaller area of the inner surface of the bottle would be available for the shearing process. The optical photograph in Figure 4C shows a homogeneous MXene ink in a large bottle after centrifugation as opposed to a dense sediment obtained in a smaller conical tube (Figure 4B). The difference between the two samples can be further illustrated by photographing a portion of this ink in a conical centrifuge tube (compare Figure 4D with Figure 4B, left). The optical photograph in Figure 4C (right) shows a much larger fraction of few-layer and monolayer $Cr_2TiC_2T_x$ flakes in the ink produced using a large polypropylene bottle compared to the precipitate that formed in a conical centrifuge tube (see Figure 4B, right). The described centrifugation-assisted delamination process is scalable, as demonstrated by the optical photographs in Figures 4E and 4F, which show a >0.5-L $Cr_2TiC_2T_x$ solution with a concentration of 17–19 mg mL^{-1}, and about 18 g dried MXene product, respectively. The exfoliated $Cr_2TiC_2T_x$ material can be processed into large-scale structures, such as continuous MXene films, as illustrated by Figure 4G.

AFM characterization of $Cr_2TiC_2T_x$ flakes

We used AFM to examine 25 distinct $Cr_2TiC_2T_x$ flakes deposited on Si/SiO_2 substrate. Figure 5A depicts a collection of largely monolayer flakes of $Cr_2TiC_2T_x$ that are uniform and have lateral sizes >10 μm. Figure 5A (right) shows a folded single-layer flake of $Cr_2TiC_2T_x$ with a lateral size of 15 μm and an overlayed height profile, with measured single-layer and bilayer thicknesses of 3.1 and 5.2 nm, respectively. Figure 5B illustrates the height profile of the collection of flakes shown in Figure 5A (left) measured along the blue dashed line, which contains up to five layers of

Please cite this article in press as: Bagheri et al., Synthesis of high-quality large $Cr_2TiC_2T_x$ MXene monolayers, their mechanical properties, *p*-type electrical transport, and positive photoresponse, MATT (2024), https://doi.org/10.1016/j.matt.2024.08.019

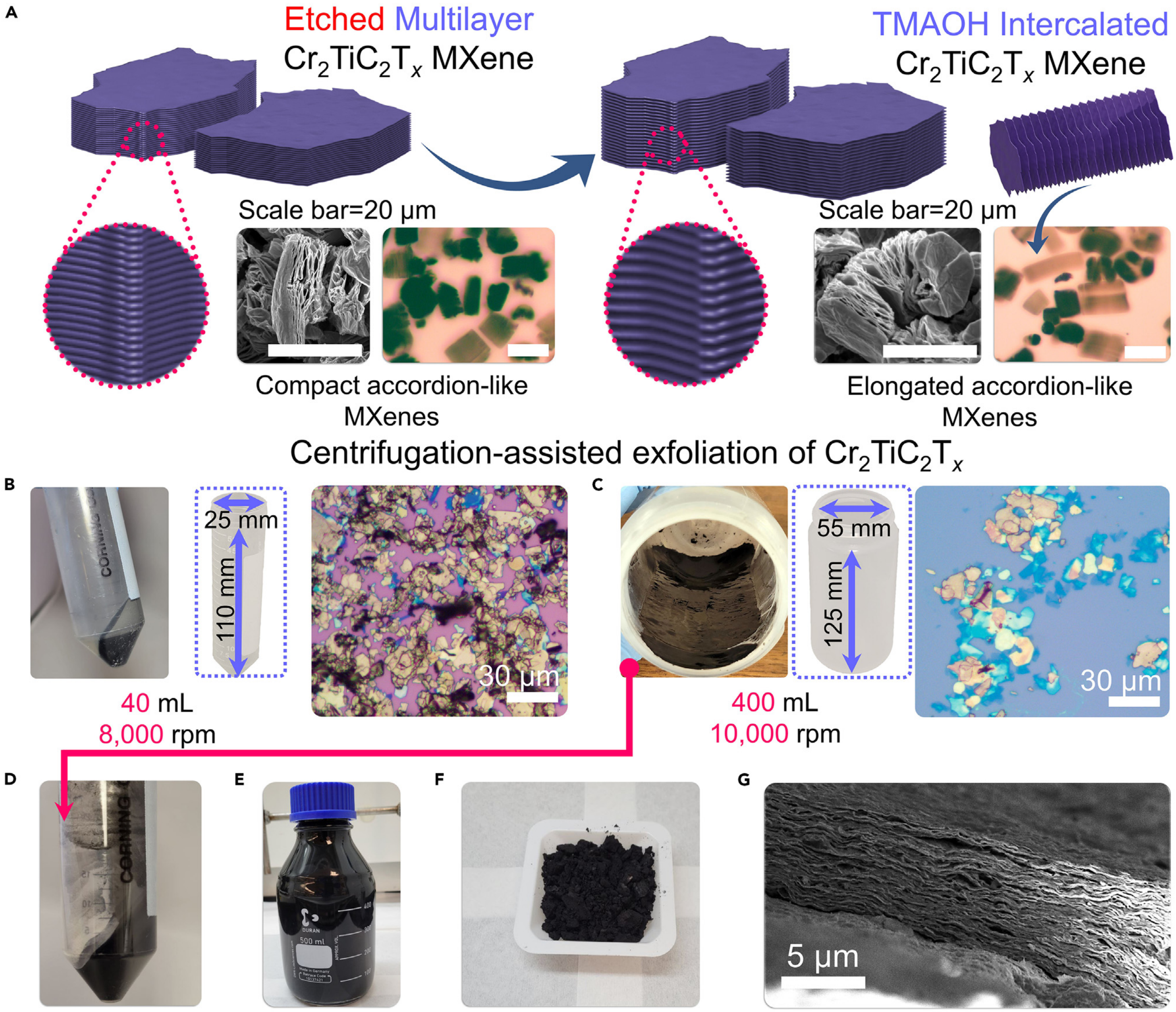

Figure 4. Intercalation and exfoliation of ML $Cr_2TiC_2T_x$ MXene

(A) Scheme of the intercalation of ML $Cr_2TiC_2T_x$ with TMAOH. SEM and optical images show $Cr_2TiC_2T_x$ MXene accordions before and after intercalation.

(B) Centrifugation of ML $Cr_2TiC_2T_x$ MXene in small conical tubes. Left: optical photograph of precipitated $Cr_2TiC_2T_x$ MXene in a conical tube after centrifugation. Center: scheme of a conical centrifuge tube with dimensions. Right: optical photograph of the $Cr_2TiC_2T_x$ precipitate dispersed over a Si/SiO_2 substrate.

(C) Centrifugation of ML $Cr_2TiC_2T_x$ MXene in large, flat-bottom bottles. Left: optical photograph of a homogeneous MXene ink in a large bottle after centrifugation. Center: scheme of a flat-bottom centrifuge bottle with dimensions. Right: optical photograph of $Cr_2TiC_2T_x$ flakes from the MXene ink dispersed over a Si/SiO_2 substrate.

(D) MXene ink that was photographed in a conical centrifuge tube for comparison with (B, left).

(E) Optical photograph of a large volume (>0.5 L) of a $Cr_2TiC_2T_x$ solution produced by centrifugation in flat-bottom polypropylene bottles.

(F) Optical photograph of 18 g of a dried MXene product produced by centrifugation in flat-bottom polypropylene bottles.

(G) Cross-sectional SEM image of a $Cr_2TiC_2T_x$ film produced from the MXene ink shown in (E).

flakes. After analyzing 103 data points, we generated the height distribution for $Cr_2TiC_2T_x$ flakes on Si/SiO_2, and the data are summarized in Figure 5C. Despite the fact that the theoretical thickness of a single-layer pristine $Cr_2TiC_2T_x$ is estimated to be around 0.98 nm (similar to $Ti_3C_2T_x$ MXene), the experimental data show that a single-layer $Cr_2TiC_2T_x$ has an AFM thickness of 2.9 nm. Similar to what we have observed in the case of other MXenes,[13,24,29] the difference between the theoretical thickness and experimental AFM height profiles could be due to the presence of small molecules, such as residual TMAOH and water, trapped underneath or between the flakes. According to the plot in Figure 5C, each additional layer on top of the first monolayer increases the AFM thickness of the entire stack by about 2.1 nm.

Please cite this article in press as: Bagheri et al., Synthesis of high-quality large $Cr_2TiC_2T_x$ MXene monolayers, their mechanical properties, *p*-type electrical transport, and positive photoresponse, MATT (2024), https://doi.org/10.1016/j.matt.2024.08.019

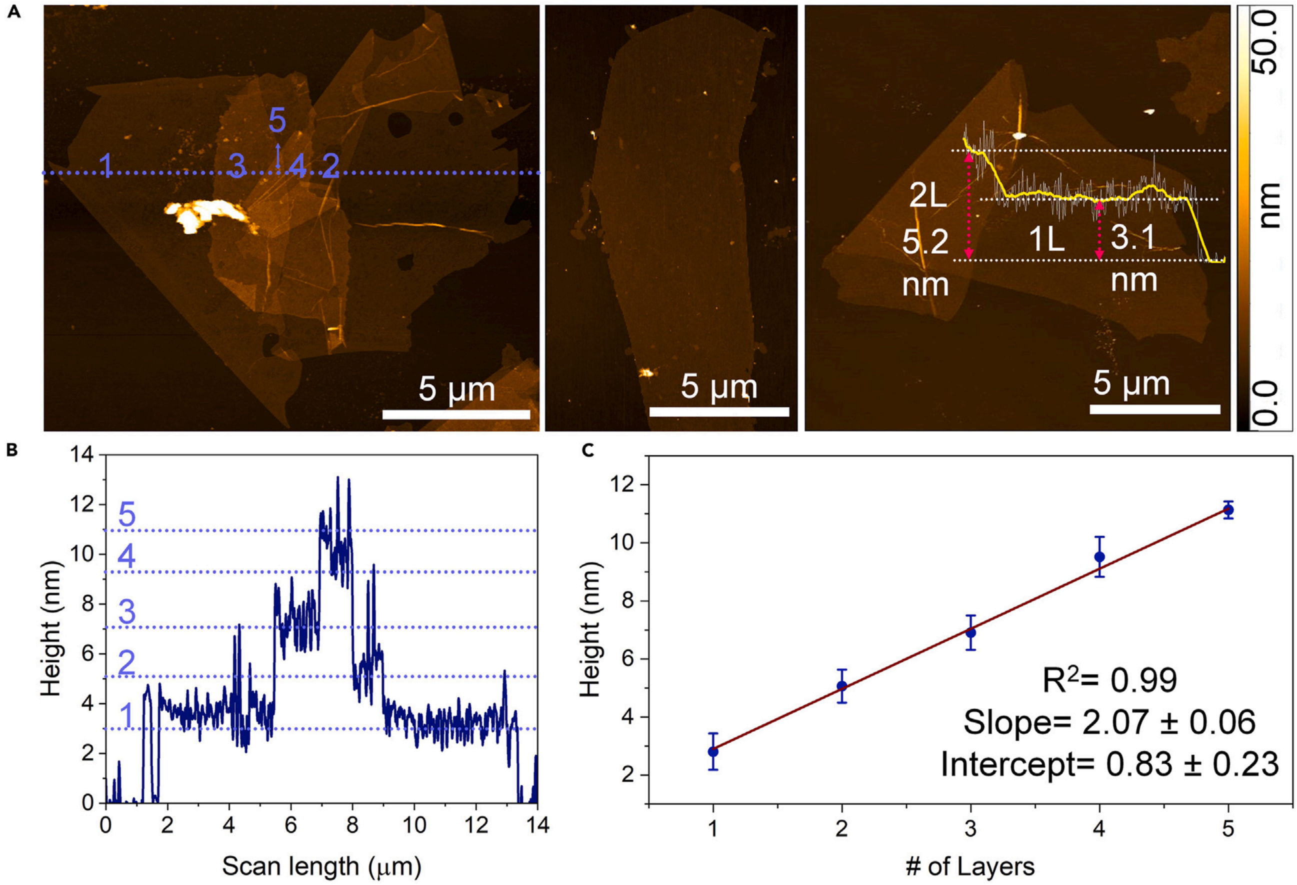

Figure 5. AFM characterization of $Cr_2TiC_2T_x$

(A) AFM images of multiple $Cr_2TiC_2T_x$ flakes on Si/SiO_2, (B) height profile of the flakes shown in (A, left) along the dotted blue line, and (C) thickness analysis data from 103 measurements of 25 $Cr_2TiC_2T_x$ flakes. Blue-colored numbers represent the number of MXene monolayers.

Electronic and optoelectronic properties of $Cr_2TiC_2T_x$ flakes

We fabricated FET devices based on $Cr_2TiC_2T_x$ as the channel material, conductive p-doped Si as the global back gate, 300-nm thermally grown SiO_2 as the gate dielectric, and Cr/Au electrodes, which were fabricated using the e-beam lithography technique. One such device is shown schematically in Figure 6A, where a monolayer $Cr_2TiC_2T_x$ flake bridges the source and drain electrodes. Figure 6B shows the topography of a six-terminal device measured by AFM, revealing the large size and high quality of the flakes synthesized by the described method and demonstrating the characteristic height of ~2.8 nm for a monolayer flake. A total of four devices were analyzed by measuring drain current (I_D) at different drain-source voltages (V_{DS}), while applying gate voltage (V_G) to the bottom electrode. Figure 6C shows linear I_D-V_{DS} characteristics of the device shown in Figure 6B, revealing ohmic contact with Cr/Au electrodes. The average conductivity (σ) across four studied devices was found to be 180 S cm^{-1} at V_{DS} = 0.1 V. As shown in Figure 6C, the I_D-V_{DS} dependences demonstrate a fairly weak modulation by a varying V_G, which is common for other MXenes, such as $Ti_3C_2T_x$[25,29] and $Nb_4C_3T_x$.[13,14] Most interestingly, Figure 6D demonstrates transfer characteristics of the same FET that reveals the *p*-type transport of $Cr_2TiC_2T_x$, the first reported for any MXene so far. In contrast, both $Ti_3C_2T_x$ and $Nb_4C_3T_x$ demonstrated *n*-type transport in similar field-effect measurements performed on devices based on monolayer MXene flakes.[13,14,25,29] As illustrated in Figure 6D, I_D decreases as V_G increases, indicating that holes are the major charge carriers in the material. We suggest that this behavior of $Cr_2TiC_2T_x$ could be related to the Cr deficiency of the synthesized material. The possible effect of Cr vacancies on the electronic properties of $Cr_2TiC_2T_x$ is considered in the section "DFT calculations of $Cr_2TiC_2T_x$." There are two arguments for the formation of Cr vacancies in $Cr_2TiC_2T_x$. First, unlike the inner Ti layers of $Cr_2TiC_2T_x$ that are isolated from the harsh acidic environment during the MXene synthesis, the outer Cr layers are exposed to etching. Second, a recent study by Michałowski and co-workers showed that the Cr_2TiAlC_2 MAX phase exhibits partial mixing between the M elements, where the outer layers are exclusively made of Cr atoms, while both Cr and Ti occupy the inner layer, with a Cr content of 10 atom %.[35] If for the Cr_2TiAlC_2 synthesis Cr and Ti are used at a stoichiometric ratio of 2:1 and some of the Cr occupies the inner layers, then there is not enough Cr to

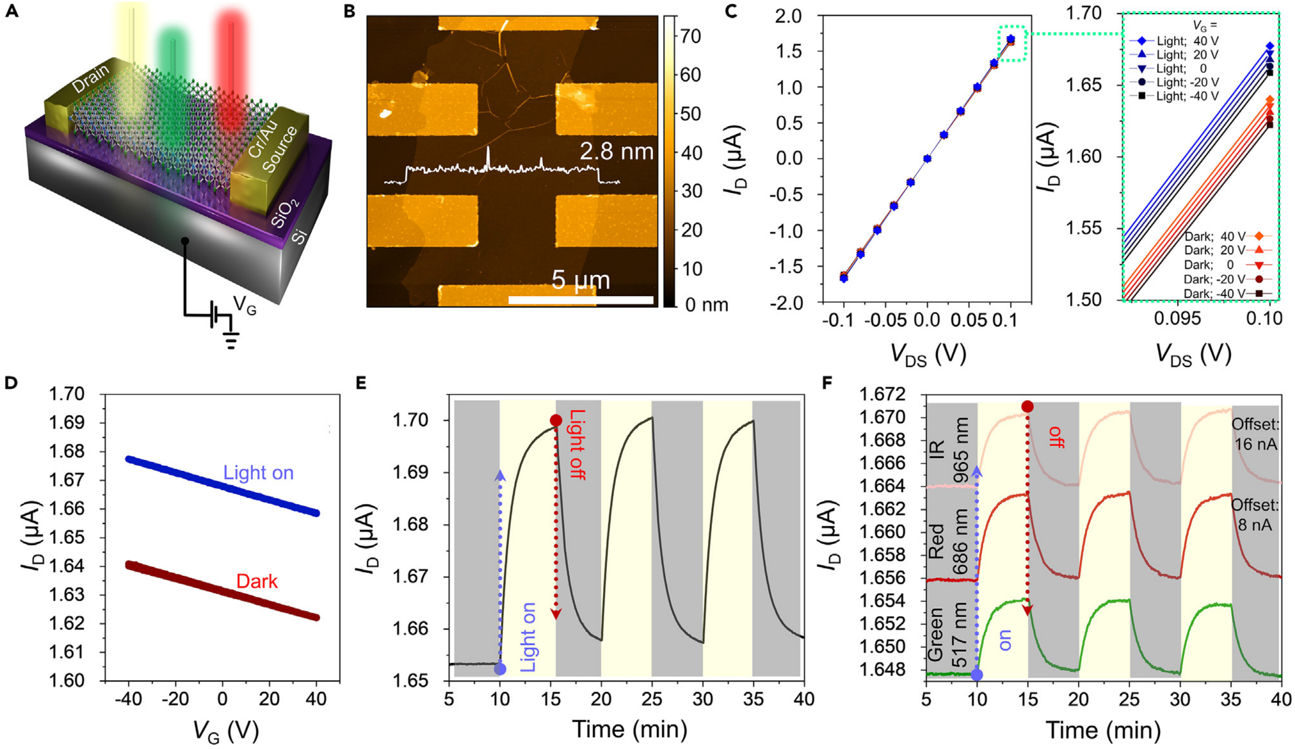

Figure 6. Electronic and optoelectronic properties of $Cr_2TiC_2T_x$

(A) Scheme of a two-terminal $Cr_2TiC_2T_x$ FET device under illumination with different lasers.

(B) AFM image of a six-terminal $Cr_2TiC_2T_x$ device. The MXene flake shows no signs of structural degradation after the device fabrication.

(C) I_D-V_{DS} curves obtained from the device shown in (B) at $V_G = -40, -20, 0, 20$, and 40 V, in the dark and under illumination with white light.

(D) I_D-V_G dependence for the same device measured at $V_{DS} = 0.1$ V.

(E) Photoresponse of the same device to white light, measured at $V_{DS} = 0.1$ V and $V_G = 0$.

(F) The modulation of photocurrent in $Cr_2TiC_2T_x$ device with three different lasers: infrared (IR, 965 nm), red (686 nm), and green (517 nm). All lasers were set to the same power of 2 mW. The measurements were performed at $V_{DS} = 0.1$ V and $V_G = 0$. The I_D axis corresponds to the electrical measurement involving the green light; the other two dependences are vertically offset for clarity by 8 nA (red laser) and 16 nA (IR laser), respectively.

completely populate the atomic positions in the outer layers, intrinsically producing Cr vacancies. SEM-EDX analysis conducted on both accordions and thin film samples of $Cr_2TiC_2T_x$ revealed atomic ratios close to 2:1 (Figure S8), as in the precursor mixture, while a higher Cr content would be needed to provide some Cr atoms for the inner layers and produce defect-free outer layers. Based on these considerations, it may be interesting to produce a MAX phase from a precursor mixture with a higher Cr content and investigate whether the resulting MXene would still have a *p*-type conductivity.

Microscopic and spectroscopic data suggest that it is unlikely that oxidation of $Cr_2TiC_2T_x$ flakes during the device fabrication could be the source of *p*-type transport. There are many reports on mildly oxidized MXene sheets exhibiting oxide nanoparticles at the flake edges[36,37] and dense coverage of flakes with oxide nanoparticles with further oxidation.[38,39] In our case, the as-prepared $Cr_2TiC_2T_x$ flakes were uniform and had very clean edges, as shown in Figures 1D and 5A. Furthermore, the microscopic investigation of the $Cr_2TiC_2T_x$ flakes after the device fabrication still shows their uniformity and clean edges, as can be seen in Figure 6B. Microscopic images of other $Cr_2TiC_2T_x$ flakes that were used in this study for electrical characterization did not show any visible signs of structural degradation either.

To further confirm the structural stability of $Cr_2TiC_2T_x$ flakes during the device fabrication, we employed X-ray photoelectron spectroscopy (XPS). During the device fabrication, we strived to minimize the exposure time of the MXene flakes to the ambient conditions, but there was still a total time of exposure to air of about 1 h between the initial deposition of $Cr_2TiC_2T_x$ on a Si/SiO_2 substrate and the final loading of a fabricated device to a vacuum probe station for electrical measurements.[40] In the process of device fabrication, the MXene flakes on Si/SiO_2 were also exposed to polymethyl methacrylate and a variety of solvents (isopropanol, acetone, methyl isobutyl ketone). To determine whether the exposure to air or lithography-related chemicals degrades $Cr_2TiC_2T_x$, we prepared a thin MXene film that was subjected to the same treatment as the flakes used for the device fabrication. The high-resolution XPS spectra for Ti and Cr elements in the as-prepared $Cr_2TiC_2T_x$ and the MXene that was subjected to a device fabrication procedure are compared in Figure S9. The XPS spectra for the as-prepared $Cr_2TiC_2T_x$ were identical to those reported and analyzed by Hantanasirisakul

Please cite this article in press as: Bagheri et al., Synthesis of high-quality large $Cr_2TiC_2T_x$ MXene monolayers, their mechanical properties, *p*-type electrical transport, and positive photoresponse, MATT (2024), https://doi.org/10.1016/j.matt.2024.08.019

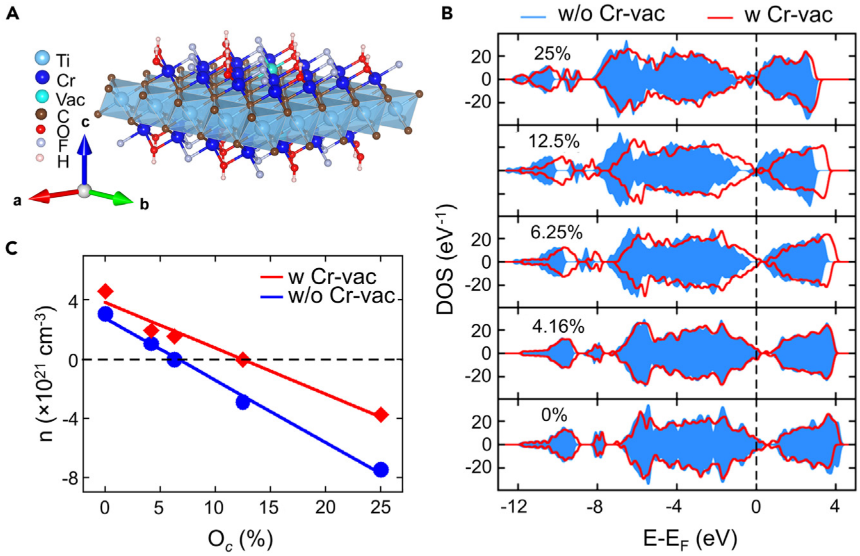

Figure 7. DFT calculations of electronic properties of $Cr_2TiC_2T_x$

(A) Representative structure of $Cr_2TiC_2T_x$ with –O, –OH, and –F functional groups and Cr vacancies (vac).

(B) DOS of $Cr_2TiC_2T_x$ plotted as a function of energy when different percentage of C is substituted by O in the presence (red) and absence (blue filled) of Cr vacancies. The Fermi level is set to zero in the x axis.

(C) Computed carrier concentration of functionalized $Cr_2TiC_2T_x$ plotted as a function of concentration of O substituting C in the presence (red) and absence (blue) of Cr vacancies. Positive and negative signs of carrier concentration represent holes and electrons, respectively.

et al.[18] Even though the Ti forms the inner metal layer in $Cr_2TiC_2T_x$, the Ti–O bonding is still possible (hence the noticeable peak at 459.7 eV) because of the previously demonstrated presence of O atoms in the C layers of this MXene material.[35] Importantly, the XPS spectra of the as-prepared and processed samples in Figure S9 look very similar, suggesting that there was no severe degradation of $Cr_2TiC_2T_x$ during the device fabrication process. Similarly, there was no difference between the XRD patterns of the as-prepared and processed samples (Figure S10), and no oxide peaks were observed after the device fabrication treatment.

From the field-effect dependence in Figure 6D, the field-effect mobility can be extracted using the following equation:

$$\mu_{FE} = \frac{\partial I_D}{\partial V_G} \frac{L}{W \cdot C_i \cdot V_{DS}} \qquad \text{(Equation 1)}$$

where W is the channel width, L is the channel length, and C_i is the capacitance between the channel and the back gate per unit area. The average mobility of holes (μ_{FE}) across four devices was found to be about 0.22 $cm^2\ V^{-1}\ s^{-1}$, which is only an order of magnitude lower than the electron mobility of $Ti_3C_2T_x$ and $Nb_4C_3T_x$ MXenes reported earlier.[13,14,25,29] The average charge carrier concentration for the tested devices was 5.2 × 10^{21} cm^{-3}; the results for each of the studied devices are provided in Table S1. This value is lower than for $Ti_3C_2T_x$[29,41] and $Nb_4C_3T_x$,[13] which have carrier concentrations on the order of 10^{22} cm^{-3},[42] but is comparable to that of Ti_3CNT_x.[9,42]

Figure 6D shows the transfer characteristics of the FET device in the dark and under light, revealing higher conductivity when illuminated by a white light. The modulation of the current is reversible, as illustrated in Figure 6E, which shows three complete cycles of illumination on and off. Furthermore, we studied the wavelength dependence of the $Cr_2TiC_2T_x$ photoresponse by illuminating the same device with laser radiation of various wavelengths at the same optical power of 2.0 mW. The results are shown in Figure 6F, where we observed the slow positive photoresponse as in the case of white light. In an earlier report,[27] we showed that $Ti_3C_2T_x$ MXene exhibited a negative photoresponse due to its metallic nature[40] so that the conductivity decreases due to scattering and local heating. The positive photoresponse of the monolayer $Cr_2TiC_2T_x$ indicates that the material has semiconductor properties. More specifically, the conductivity of semiconductors increases with temperature, and as the MXene material absorbs light and heats up, it becomes more conductive, as we observe experimentally (Figures 6D–6F). Because the photoresponse measurements were performed in vacuum, the heating of $Cr_2TiC_2T_x$ under white light or laser illumination did not cause its degradation, unlike the case where MXenes are annealed in air in the presence of oxygen and water molecules.[37,38] As a result, the photoresponse cycles in Figure 6E and 6F are very reproducible, suggesting the stability of $Cr_2TiC_2T_x$ under the experimental conditions.

DFT calculations of $Cr_2TiC_2T_x$

To gain insights into the electronic and transport properties of $Cr_2TiC_2T_x$, we performed DFT calculations. Figure 7A shows a $Cr_2TiC_2T_x$ slab with –O, –OH, and –F surface functional groups in a 1:2:5 ratio, which is similar to that determined in a recent study that used secondary mass ion spectroscopy measurements.[35] That study also established that some of the C atoms in the $Cr_2TiC_2T_x$ structure may be substituted with O,[35] so we included the possible presence of O atoms in the structural model as well. Thus, in the density of states (DOS) calculations, we investigated the effect of two parameters on the electronic properties of $Cr_2TiC_2T_x$: the presence of Cr vacancies and the possible substitution of C atoms in the MXene structure with O. The corresponding DOS plots as a function of energy for $Cr_2TiC_2T_x$ with different percentages of O substituting C (O_C) in the structure and also with and without Cr vacancies are presented in Figure 7B. As shown in the bottom panel in Figure 7B, for the pristine material without O substitution, the Fermi level crosses the valence band of a gapped electronic structure, suggesting a *p*-type semiconducting character. Figure 7B shows that the Fermi level energy position increases with the concentration of O_C; it lies at the middle of the band gap when the O_C

Please cite this article in press as: Bagheri et al., Synthesis of high-quality large $Cr_2TiC_2T_x$ MXene monolayers, their mechanical properties, *p*-type electrical transport, and positive photoresponse, MATT (2024), https://doi.org/10.1016/j.matt.2024.08.019

concentration is 6.25% (center panel) and eventually crosses the conduction band, turning the material into an *n*-type semiconductor.

Like other researchers in the literature,[43–45] we also considered the effect of individual (–O, –F, and –OH) functional groups and their equal mixtures, –O/–F and –F/–OH, on the electronic properties of $Cr_2TiC_2T_x$ (see Figure S11). The pristine MXene featuring either –O surface functional groups or a mix of –O and –F exhibits *p*-type conductivity and the Fermi level crosses bands with an estimated carrier concentration of about 4×10^{21} cm^{-3}. Despite the presence of a gap indicative of a semiconducting nature, such carrier concentration potentially indicates metallic behavior in electrical measurements. Notably, Zhang et al.[46] obtained similar computational plots and interpreted them as suggesting metallic character of $Cr_2TiC_2T_x$. However, when the surface functional groups are altered to –OH, –F, or a mix of –OH and –F, the pristine MXene demonstrates semiconducting properties. Furthermore, in the presence of Cr vacancies at 1.67 atom % (corresponding to 2 vacancies in a 120-atom supercell), $Cr_2TiC_2T_x$ becomes *p*-type, with the Fermi level intersecting a substantial portion of the valence band for all investigated surface terminations.

Collectively, these observations show that the Cr vacancy (V_{Cr}) behaves as an acceptor defect, while the O_C behaves as a donor defect. The Cr vacancy donates holes and promotes the *p*-type character, while O_C donates electrons and promotes the *n*-type character. Figure 7C shows the evolution of carrier concentration as a function of the O_C concentration with and without V_{Cr}. As expected, when V_{Cr} is added, the hole (electron) concentration increases (decreases). Formation energy calculation shows that the O_C defects are exothermic and form spontaneously ($\Delta H = -4.2$ eV/O_C with respect to the oxygen molecule), which is consistent with the experimental observation.[35] The Cr vacancies, while they may form in a harsh acidic environment during the $Cr_2TiC_2T_x$ synthesis, are endothermic ($\Delta H = 1.3$ eV/V_{Cr} with respect to Cr metal) and require additional energy to form at the standard temperature and pressure. As we discuss above, there is also a possibility that the Cr vacancies form during the MAX phase synthesis, as some of the Cr atoms may occupy the inner layers instead of the outer layers.[35] Overall, the computational results predict that depending on the concentrations of both V_{Cr} and O_C (Figure 7C) and the surface terminations (Figure S11), $Cr_2TiC_2T_x$ could be tuned from *p*- to *n*-type. In our experiments, the material was *p*-type, as evidenced by the modulation of the I_D by the V_G with a negative slope (Figure 6D). However, following these computational results, it would be potentially interesting to systematically investigate the effect of these parameters (V_{Cr}, O_C, and surface terminations) on the electronic properties of $Cr_2TiC_2T_x$ to experimentally demonstrate the tunability of its *p*-/*n*-type characteristics.

Elastic properties of $Cr_2TiC_2T_x$

We tested the elastic properties of $Cr_2TiC_2T_x$ using nanoindentation technique, which involves indenting a suspended material with a sharp AFM probe and measuring the indentation depth and the applied force.[13,30] The samples for the nanoindentation experiment were prepared by transferring freshly synthesized $Cr_2TiC_2T_x$ flakes on a prefabricated Si/SiO_2 substrate with 1.2-μm wide and 300-nm deep microwells. The process followed the protocol established in our earlier works.[13,30] The transfer was performed by depositing concentrated MXene solution on a polydimethylsiloxane (PDMS) stamp, followed by drying to form a thin film of MXene flakes. The PDMS stamp was flipped so that the flakes faced downward and then was placed on the Si/SiO_2 substrate, followed by a gentle press. Due to the relatively large diameter of the microwells, it was important to peel off the PDMS stamp from the Si/SiO_2 substrate very slowly to avoid fracturing the membranes. Several monolayer and bilayer $Cr_2TiC_2T_x$ flakes covering the microwells were located using an optical microscope. The AFM image of a representative MXene membrane and the height profile across the center of the microwell are shown in Figure 8A. The flake adheres to the walls of the microwell and stretches at a depth of about 20–30 nm, which is well above the bottom of the well.

The scheme of the nanoindentation experiment is shown in Figure 8B, where a sharp AFM tip positioned above the center of a microwell slowly pushes down over the MXene flake. During the experiment, both applied force (F) and deflection (δ) are measured. The experiment is repeated several times for different F's until the membrane fractures. The resulting F-δ curves for the monolayer $Cr_2TiC_2T_x$ flake recorded for different Fs are shown in Figure 8C. Each new F-δ curve perfectly follows the previous one, indicating that the membrane remains elastic and does not slide from the edges. Several experiments were performed for monolayer and bilayer flakes, and the comparison of F-δ curves for monolayer and bilayer $Cr_2TiC_2T_x$ flakes is shown in Figure 8D. Similar to previous reports,[13,30,47,48] we fitted the experimental F-δ data using the formula:

$$F = \sigma_0^{2D}\pi\delta + E^{2D}\frac{q^3\delta^3}{r^2} \qquad \text{(Equation 2)}$$

where σ_0^{2D} represents pre-stress in the membrane, E^{2D} is the 2D elastic modulus, and $r = 600$ nm is the radius of the well.[47,48] The dimensionless constant q is related to Poisson's ratio v as $q = (1.049 - 0.15v - 0.16v^2)^{-1}$. Due to the structural similarity between $Cr_2TiC_2T_x$ and $Ti_3C_2T_x$, we utilized the Poisson's ratio value for $Ti_3C_2T_x$ of 0.227,[49] resulting in $q = 0.9933$. The first term in Equation 2 corresponds to the linear bending and prestrained deflection of the membrane and is valid for small loads. The second term corresponds to the nonlinear membrane behavior during large loads and is characterized by a cubic $F \sim \delta^3$ relationship with a coefficient of E^{2D}. Other nonlinear effects in Equation 2 can be ignored if the AFM tip radius is much smaller than the radius of a well (i.e., $r_{tip}/r \ll 1$).[47,48] In our case, the diameter of the well measured by AFM is $a = 2r =$ 1,200 nm, and according to the manufacturer's specifications, the AFM tip radius is 7 nm, which results in $r_{tip}/r = 0.006 \ll 1$. Figure 8D shows the experimental and fitting curves for monolayer and bilayer MXene flakes, with the goodness of fit $R^2 > 0.995$, which is an indicator that the utilized model is appropriate.

In our work, we measured 12 experimental F-δ curves from 3 monolayer $Cr_2TiC_2T_x$ flakes and 24 experimental curves from 3 bilayer flakes. The results for all experiments are summarized in the histogram plot in Figure 8E. For monolayer $Cr_2TiC_2T_x$, the E^{2D} elasticity ranged from 187 to 260 N m^{-1}, with an average

Please cite this article in press as: Bagheri et al., Synthesis of high-quality large $Cr_2TiC_2T_x$ MXene monolayers, their mechanical properties, *p*-type electrical transport, and positive photoresponse, MATT (2024), https://doi.org/10.1016/j.matt.2024.08.019

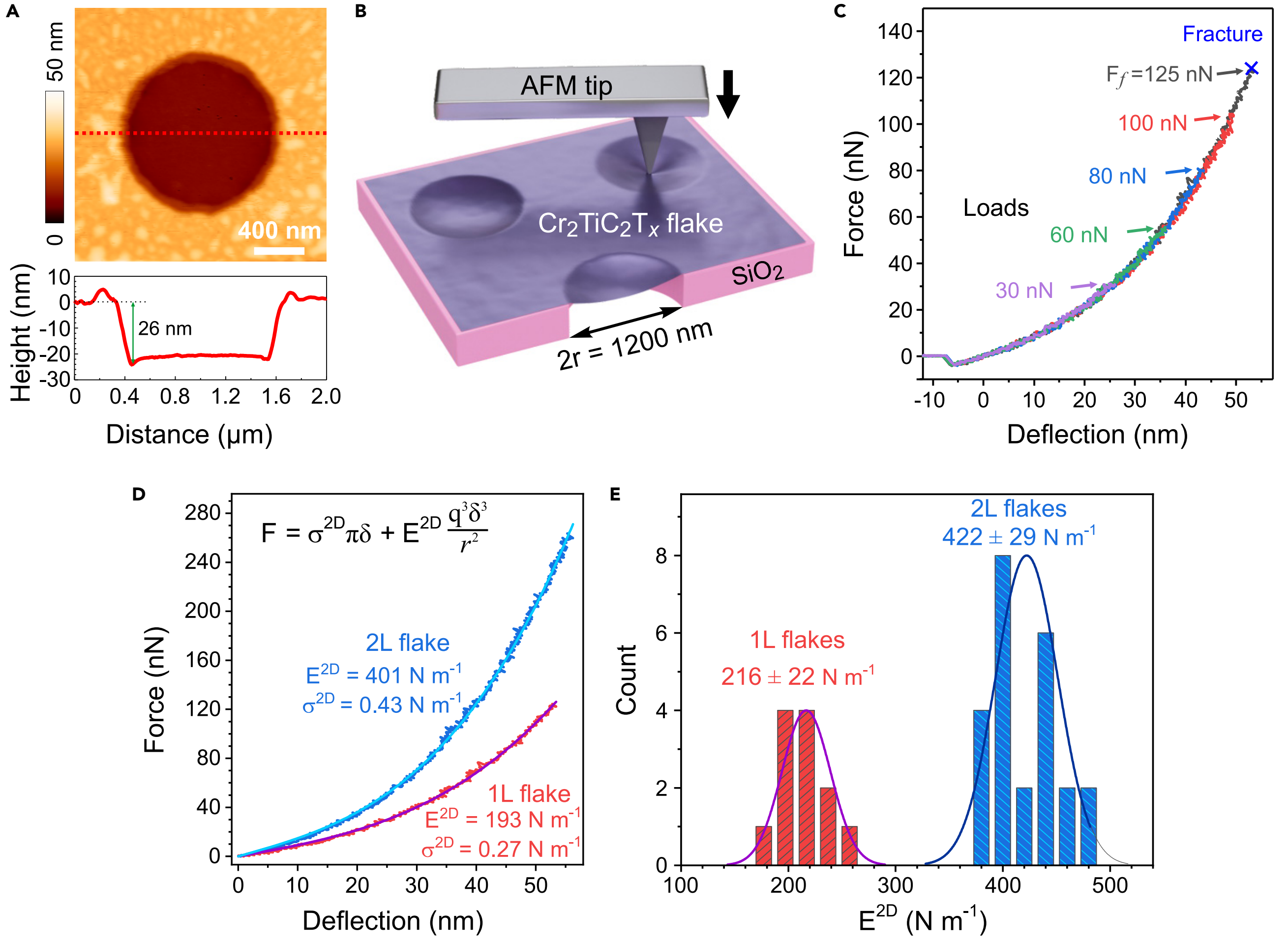

Figure 8. Characterization of mechanical properties of $Cr_2TiC_2T_x$ flakes

(A) Top: AFM image of a $Cr_2TiC_2T_x$ flake covering a 1,200-nm-wide microwell in a Si/SiO_2 substrate. Bottom: AFM height profile measured along the dashed line.

(B) Schematic image of the nanoindentation experiment using AFM to stretch suspended $Cr_2TiC_2T_x$ membrane.

(C) Force-deflection curves produced for a monolayer $Cr_2TiC_2T_x$ membrane at different loads. Fracture force is indicated by the blue cross.

(D) Force-deflection curves for monolayer (1L) and bilayer (2L) $Cr_2TiC_2T_x$ membranes and the least squares fits (solid lines) to the experimental data by Equation 2.

(E) Histogram of the elastic stiffness values for 1L and 2L $Cr_2TiC_2T_x$ membranes. The solid line represents a Gaussian fit to the data.

of 216 ± 22 N m^{-1}, and for bilayer flakes, E^{2D} elasticity ranged from 384 to 473 N m^{-1}, with an average of 422 ± 29 N m^{-1}. The 2D elastic modulus of bilayer MXene flakes is exactly twice that of monolayer flakes, suggesting strong interaction between layers that is likely associated with the hydrogen bonding between the surface terminal groups of $Cr_2TiC_2T_x$. Similar effects were observed for overlapping graphene oxide (GO) membranes[50] and $Ti_3C_2T_x$ and $Nb_4C_3T_x$ MXene membranes.[13,30]

The effective Young's modulus E_{Young} can be calculated by dividing E^{2D} by the membrane thickness. For the effective thickness of a monolayer $Cr_2TiC_2T_x$ we used 0.98 nm, the previously determined effective thickness of monolayer $Ti_3C_2T_x$,[30] considering the structural similarities of these two MXenes and identical atomic radii of Ti and Cr. The effective modulus for the $Cr_2TiC_2T_x$ membrane is 220 ± 22 GPa, which is lower than the previously measured Young's moduli for $Ti_3C_2T_x$ (330 GPa)[30] and $Nb_4C_3T_x$ (386 GPa)[13] MXenes. However, the effective Young's modulus of $Cr_2TiC_2T_x$ is still comparable to those of many other 2D materials, such as GO[50] and transition metal dichalcogenides (TMDs),[48,51,52] which were tested in similar nanoindentation experiments. Considering that GO is widely used for a variety of mechanical applications, such as fibers, protective coatings, and reinforced composite materials, $Cr_2TiC_2T_x$ should be suitable for similar uses as well. Furthermore, the lower Young's modulus of $Cr_2TiC_2T_x$ compared to the previously tested MXenes could also be related to the Cr vacancies, suggesting that the mechanical properties may be improved with the further optimization of the synthetic procedure.

Conclusions

In summary, we reported optimized conditions for the synthesis of $Cr_2TiC_2T_x$, which produces large high-quality flakes in bulk quantities. The use of a sieved large-particle fraction of the Cr_2TiAlC_2 MAX phase and the reduction of impurities using an acid treatment were shown to have positive effects on the quality of MXene products. Also, the delamination yield and the flake size were shown to

Please cite this article in press as: Bagheri et al., Synthesis of high-quality large $Cr_2TiC_2T_x$ MXene monolayers, their mechanical properties, *p*-type electrical transport, and positive photoresponse, MATT (2024), https://doi.org/10.1016/j.matt.2024.08.019

depend on the centrifugal forces exerted on etched particles, resulting in the shearing effect. With the optimized synthetic procedure, it was possible to produce high-quality monolayer flakes of $Cr_2TiC_2T_x$, with lateral sizes exceeding 15 μm.

The physical measurements performed on large monolayer flakes of $Cr_2TiC_2T_x$ demonstrate that it has unique properties compared to other established MXene materials. Field-effect electrical measurements performed on devices patterned on monolayer $Cr_2TiC_2T_x$ flakes revealed an average conductivity of 180 S cm^{-1} and *p*-type transport properties, while MXene materials, such as $Ti_3C_2T_x$ and $Nb_4C_3T_x$, demonstrated *n*-type behavior in similar measurements. When illuminated with visible or infrared light, $Cr_2TiC_2T_x$ devices show positive photoresponse in contrast to the negative photoresponse that was recently reported for $Ti_3C_2T_x$ monolayers. We suggest that the *p*-type behavior is related to the Cr vacancies, while the positive photoresponse is consistent with the semiconducting character of $Cr_2TiC_2T_x$. The fact that many of the electronic and optoelectronic characteristics of $Cr_2TiC_2T_x$ appear to be complementary to the more established MXenes, notably $Ti_3C_2T_x$, suggests possible property engineering in various composites and layered heterostructures of different MXene materials. For example, different MXenes may form *p-n* junctions or electronic structures with tunable photoresponses. $Cr_2TiC_2T_x$ has a respectable effective Young's modulus of 220 ± 22 GPa, which is comparable to GO and TMDs and therefore suggests the utility of this MXene for a variety of mechanical applications. This work demonstrates the importance of optimization of synthetic procedures for other emerging MXene materials, some of which may also reveal unique properties if measured on a single-flake level.

Finally, the computational results of this study suggest several promising directions for the further exploration of this MXene material. DFT results provide insights into the *p*-type character of $Cr_2TiC_2T_x$ and further predict that this is potentially a tunable *p-/n*-type system depending on the concentrations of Cr vacancies, O_C substitution in Cr_2TiC_2 layers, and surface terminations. It may be interesting to systematically investigate the effect of these parameters (V_{Cr}, O_C, and surface terminations) on the electronic properties of $Cr_2TiC_2T_x$ to experimentally demonstrate the tunability of its *p-/n*-type characteristics. In particular, it may be interesting to produce a Cr_2TiAlC_2 MAX phase from a precursor mixture with a higher Cr content compared to the stoichiometric Cr:Ti ratio of 2:1 and investigate whether the resulting MXene would still have a *p*-type conductivity.

EXPERIMENTAL PROCEDURES

Reagents and materials

Ti (99%, 325 mesh), Al (99%, 325 mesh), graphite (C, 99%, 325 mesh), and Cr (99.9%, 325 mesh) were purchased from Alfa Aesar. Concentrated HCl (37%) and HF (48%–51%) were purchased from VWR. Potassium carbonate was purchased from Sigma-Aldrich and used to neutralize acids. TMAOH solutions (25 wt. % in water and 25 wt. % in methanol) were purchased from Sigma-Aldrich. All chemicals were used as received.

Synthesis

Cr_2TiAlC_2 MAX phase synthesis

Cr_2TiAlC_2 MAX phase was synthesized according to the previous report, with minor modifications.[18] In a typical reaction, a stoichiometric mixture of the elemental components was ground using a mortar and pestle, transferred into an alumina crucible, heated to 1,450°C at a 3°C/min ramping rate under the 450-sccm flow of Ar, and then annealed in the same atmosphere for 8 h. The prepared Cr_2TiAlC_2 was crushed, ball milled (500 rpm, 3–5 min), sieved, and washed in 9 M HCl (10 mL of acid for every 1 g of material) for 1–2 h to reduce the amount of Cr-based impurities.

Sonication-assisted $Cr_2TiC_2T_x$ MXene synthesis

$Cr_2TiC_2T_x$ was synthesized using a mixture of HCl and HF as the etchant.[18] A total of 2 g of MAX phase was slowly dispersed in a mixture of 6 mL HF, 9 mL HCl, and 15 mL H_2O and stirred at 35°C for 42 h (400 rpm, 2-in stir bar). Next, the ML $Cr_2TiC_2T_x$ was washed until pH 6 was reached and then used for the intercalation and delamination steps. A solution of 1 mL TMAOH (25% in water) and 9 mL of deionized (DI) water was used for the intercalation. The mixture of $Cr_2TiC_2T_x$ and the TMAOH solution was stirred at room temperature for 10 h. Next, the solution was centrifuged at 10,000 rpm multiple times, and finally probe sonicated for 30 min (4 s alternate on-off cycle). The mixture was centrifuged at 3,500 rpm for 1 h, resulting in the supernatant with monolayer and few-layer flakes. The sample collected in this process was comparable to the original report regarding quality and flake size.[18]

Large-flake $Cr_2TiC_2T_x$ MXene synthesis

MAX phase sieving. Initially, the MAX phase crystals were prepared according to the method described in the section "Cr_2TiAlC_2 MAX phase synthesis." MAX phase powder was first sieved with a series of Advantech testing sieves, with mesh sizes from 150 to 25 μm, and then the powder fraction with particle sizes <25 μm was sieved using Endecotts microplate sieves with mesh sizes of 20 and 10 μm. The Cr_2TiAlC_2 MAX phase fraction with particles in the range of 30–40 μm was used as the precursor for the next step (see Figure S3).

Etching conditions. MAX phase (6 g) was slowly added to the etching solution containing 18 mL HF, 32 mL HCl, and 45 mL H_2O and stirred using a 2-in stir bar at 600 rpm for 48 h at room temperature. The stirring rpm is important, and the choice of stir bar (size and weight) will affect the synthesis yield. Next, the etched sample was washed to pH 7 before intercalation (see Figure S5). We also performed the synthesis for 24 h as part of the preliminary experiments (see Figure S4).

Intercalation process. For intercalation, we used a solution prepared by adding 2 mL 25% TMAOH in methanol to 8 mL H_2O. For the initial 2 g of MAX phase, 24-h intercalation was proved necessary for a high-yield delamination at room temperature. The delamination was performed while stirring at 750 rpm using a 1-in stir bar. We also tested a higher concentration of TMAOH in an intercalant solution (2.8 mL 25% TMAOH in methanol mixed with 7.2 mL H_2O), which resulted in the degradation of $Cr_2TiC_2T_x$ flakes (see Figure S6). For a lower concentration of TMAOH (1 mL 25% solution of TMAOH in methanol and 9 mL H_2O), we observed a lower yield of delamination.

Centrifugation. After intercalation, the solution was continuously centrifuged at 10,000 rpm (washed with DI water to pH 7). It is important to use a 500-mL centrifuge tube with no conical curvature and a high wall surface area. We used 500-mL Nalgene PPCO centrifuge bottles with sealing closure. These bottles allow for a shearing effect during centrifugation, which helps the delamination process (see Figure 4C). With conventional 50-mL Falcon tubes we observed stacking of the intercalated particles (see Figure 4B).

Finally, the $Cr_2TiC_2T_x$ from the last step was delaminated in 50-mL DI water through mild shaking for 20–30 min and centrifuging at 1,500 rpm for 5 min to obtain flakes with a 5- to 15-μm lateral size. Overall, 6 g of the MAX phase produced 50 mL of a large-flake MXene suspension with a concentration of about 20 mg mL^{-1}, which translates into a yield of ~20%.

Characterization

$Cr_2TiC_2T_x$ flakes were imaged using an FEI field-emission scanning electron microscope at the accelerating voltage of 5 kV. A concentrated MXene suspension was drop cast on a Si/SiO_2 substrate and dried in air. Next, the substrate was cut in half to reveal the cross-section of the film and loaded into the SEM instrument for imaging. An FEI Tecnai Osiris transmission electron microscope equipped with a high-angle annular dark-field imaging detector and an X-FEG high-brightness Schottky field-emission gun was used to image the $Cr_2TiC_2T_x$ flakes. The accelerating voltage was 200 kV. For TEM characterization, a sample of $Cr_2TiC_2T_x$ was diluted in ethanol, and then the suspension was drop cast on a lacey carbon-coated Cu TEM grid (Ted Pella). XRD patterns

Please cite this article in press as: Bagheri et al., Synthesis of high-quality large $Cr_2TiC_2T_x$ MXene monolayers, their mechanical properties, *p*-type electrical transport, and positive photoresponse, MATT (2024), https://doi.org/10.1016/j.matt.2024.08.019

of prepared samples were collected using a PANalytical Empyrean diffractometer in the Bragg-Brentano configuration, with Ni-filtered Cu Kα radiation operated at 45 kV and 40 mA. AFM of $Cr_2TiC_2T_x$ flakes was performed using a Bruker Dimension Icon atomic force microscope in a tapping mode. The XPS analysis of the samples was carried out using a Thermo Scientific K-Alpha X-ray photoelectron spectrometer with monochromatic Al Kα (1,486.6 eV) radiation.

Electrical characterization of individual MXene flakes

A droplet of an aqueous solution of $Cr_2TiC_2T_x$ flakes was drop cast on a Si/SiO_2 substrate, a heavily *p*-doped Si substrate covered with a 300-nm-thick layer of SiO_2, and dried in air. A Zeiss Supra 40 field-emission scanning electron microscope and a Raith pattern generator were used for electron beam lithography to pattern electrodes on the $Cr_2TiC_2T_x$ flakes. An AJA electron beam evaporator at a base pressure of $\sim 8 \times 10^{-9}$ Torr was used to evaporate 3 nm Cr and then 20 nm Au, both at a rate of 0.03 nm/s.

The $Cr_2TiC_2T_x$ devices were measured in a Lake Shore TTPX cryogenic probe station at a base pressure of about 2×10^{-6} Torr. Prior to the electrical measurements, the devices were kept in the evacuated chamber of a probe station for at least 2 days to minimize the effect of surface adsorbates.[27,53] The electrical measurements were performed using an Agilent 4155C semiconductor parameter analyzer that was operated using a National Instruments LabView code.

For the white light illumination of the $Cr_2TiC_2T_x$ devices, we used a 150-W Philips 14501 DDL 20-V halogen light bulb; the emission spectrum of this bulb was reported elsewhere.[27,54] A Thorlabs S120C standard photodiode power sensor was used to measure the maximum light intensity at 600 nm of 6 mW cm^{-2}.

For the wavelength-dependent photoconductivity measurements, we used a Thorlabs multichannel laser source with 517-nm (green), 686-nm (red), and 965-nm (infrared) outputs. For each laser, the power was standardized at 2 mW. A laser spot with a diameter of about 5 mm was aligned on a $Cr_2TiC_2T_x$ device using an optical fiber and collimator.

Nanoindentation experiments

Surface topography imaging and force-deflection curve measurements of $Cr_2TiC_2T_x$ membranes were performed on an Asylum Research MFP-3D system. Single crystal diamond tips (D80, SCDprobes) with a tip radius of 5–10 nm and a spring constant $\sim$3.5 N m^{-1}, according to the manufacturer's specifications, were used for the experiments. The spring constant of each AFM cantilever was calibrated via the thermal noise method before the indentation experiments. During the experiments, the *z*-piezo displacement speed was controlled at a rate of 100 nm s^{-1}. Different rates ranging from 50 to 1,000 nm s^{-1} were also tested and showed no clear difference for the force-deflection curves.

Analysis of force-indentation curves

During the indentation experiments, the cantilever bending and *z*-piezo displacement were recorded as the tip moved downward. The cantilever bending was calibrated by first measuring a force-displacement curve on a hard Si/SiO_2 surface. The loading force was obtained from the cantilever bending multiplied by the cantilever spring constant, and the deflection of the membrane was obtained by subtracting the cantilever bending from the *z*-piezo displacement. In the experimental force-deflection data, there is a negative force section due to the tip jump-to-surface effect, where the tip snaps down to the membrane attracted by van der Waals forces when it is very close to the surface. We extrapolated the zero-force line in the force-deflection dependence prior to snapping until it crossed the curve. We considered this point as the origin, where the force and displacement are both zero, which is necessary to obtain the correct force-deflection relationship.

DFT calculations

Computational details

DOS for $Cr_2TiC_2T_x$ was studied using spin polarized DFT as applied in the Vienna *Ab Initio* Simulation Package (VASP).[55,56] The electron-ion potential was approximated using the projected augmented plane wave (PAW) method.[57] The exchange and correlation potential was calculated using the generalized density approximation (GGA). In these calculations, we used a kinetic energy cutoff of 540 eV for the plane wave expansion of the PAWs and a 6×6×2 grid of *k* points for the Brillouin zone integration.[58] The exchange and correlation, beyond GGA, were considered by introducing an onsite Coulomb repulsion with a Hubbard U = 4 eV for Cr 3d orbitals and 3 eV for Ti 3d orbitals in rotationally invariant formalism,[59] as implemented in VASP, so as to incorporate a strong electron correlation in 3d electrons. The van der Waals interaction (DFT-D3) was included in the calculations to describe the interlayer separation.[60]

Determination of lattice parameters of functionalized MXenes

Surface functional groups (–O, –F, –OH, and mixed –F/–O and –F/–OH terminations) were placed on energetically favorable hollow sites, right above the Ti atoms.[46] In the functional group –OH, the H atom was placed directly on top of the O atom situated in a hollow site. In the case of the mixed –F/–O termination, both F and O were placed in alternate hollow sites. Similarly, we placed –F and –OH in alternate hollow sites in the mixed –F/–OH case. In-plane lattice constants, *a*, were then determined by finding the minima of energy using the energy vs. *a* curve. Table S2 shows the calculated lattice parameters. For MXenes terminated with –OH, –F, and their mixture, the calculated lattice constants were slightly larger than for nonfunctionalized Cr_2TiC_2. In contrast, the lattice parameters were slightly smaller for MXenes with –O and –F/–O terminations. While we used these calculated lattice constants, it is possible to use the parameters of nonfunctionalized Cr_2TiC_2, which does not change the results qualitatively as the difference is small.

RESOURCE AVAILABILITY

Lead contact

The lead contact is Alexander Sinitskii (sinitskii@unl.edu).

Materials availability

MXene samples used in this study are available upon request from the Sinitskii laboratory at the University of Nebraska-Lincoln.

Data and code availability

Materials characterization data are available from the Sinitskii laboratory at the University of Nebraska-Lincoln. Calculation data and details are available from the Paudel laboratory at the South Dakota School of Mines and Technology.

ACKNOWLEDGMENTS

The work was supported by the National Science Foundation through awards OIA-2044049 (MXene synthesis) and OSI-2329159 (device fabrication and characterization). Some experiments were performed using the instrumentation at the University of Nebraska-Lincoln instrumentation facilities supported by the National Science Foundation (award ECCS-2025298), the Nebraska Research Initiative, and the Nebraska Center for Energy Sciences Research. The DFT work at the South Dakota School of Mines and Technology was supported by the South Dakota Board of Regents through a competitive research grant.

AUTHOR CONTRIBUTIONS

Conceptualization, A.S. and S.B. Material synthesis, S.B. and M.I.K. Material characterization, S.B. AFM analysis, M.J.L. and R.K. Fabrication of FET devices, M.J.L. Electrical and optoelectrical measurements, M.J.L. Fabrication of MXene membranes, A.L. Nanoindentation experiments, H.L. and A.G. DFT calculations, K.A. and T.R.P. Investigation and validation, S.B., A.L., H.L., and M.J.L. Data analysis of the nanoindentation experiments, A.L. and H.L. Visualization, S.B., A.L., and A.S. Writing – original draft, S.B. and A.S. Writing – review & editing, S.B. and A.S. Supervision, A.S. All authors have approved the final version of the manuscript.

DECLARATION OF INTERESTS

The authors declare no competing interests.

SUPPLEMENTAL INFORMATION

Supplemental information can be found online at https://doi.org/10.1016/j.matt.2024.08.019.

Received: June 15, 2023
Revised: July 8, 2024
Accepted: August 19, 2024
Published: October 1, 2024

REFERENCES

1. Gogotsi, Y., and Anasori, B. (2019). The Rise of MXenes. ACS Nano *13*, 8491–8494.
2. Anasori, B., and Gogotsi, Y. (2019). 2D Metal Carbides and Nitrides (MXenes): Structure, Properties and Applications (Springer International Publishing).
3. Naguib, M., Kurtoglu, M., Presser, V., Lu, J., Niu, J., Heon, M., Hultman, L., Gogotsi, Y., and Barsoum, M.W. (2011). Two-Dimensional Nanocrystals Produced by Exfoliation of Ti_3AlC_2. Adv. Mater. *23*, 4248–4253.
4. Naguib, M., Mashtalir, O., Carle, J., Presser, V., Lu, J., Hultman, L., Gogotsi, Y., and Barsoum, M.W. (2012). Two-Dimensional Transition Metal Carbides. ACS Nano *6*, 1322–1331.
5. Xue, N., Li, X., Han, L., Zhu, H., Zhao, X., Zhuang, J., Gao, Z., and Tao, X. (2022). Fluorine-free synthesis of ambient-stable delaminated Ti_2CT_x (MXene). J. Mater. Chem. A *10*, 7960–7967.
6. Mashtalir, O., Lukatskaya, M.R., Zhao, M.-Q., Barsoum, M.W., and Gogotsi, Y. (2015). Amine-Assisted Delamination of Nb_2C MXene for Li-Ion Energy Storage Devices. Adv. Mater. *27*, 3501–3506.
7. Halim, J., Cook, K.M., Naguib, M., Eklund, P., Gogotsi, Y., Rosen, J., and Barsoum, M.W. (2016). X-ray photoelectron spectroscopy of select multi-layered transition metal carbides (MXenes). Appl. Surf. Sci. *362*, 406–417.
8. Naguib, M., Halim, J., Lu, J., Cook, K.M., Hultman, L., Gogotsi, Y., and Barsoum, M.W. (2013). New Two-Dimensional Niobium and Vanadium Carbides as Promising Materials for Li-Ion Batteries. J. Am. Chem. Soc. *135*, 15966–15969.
9. Hantanasirisakul, K., Alhabeb, M., Lipatov, A., Maleski, K., Anasori, B., Salles, P., Ieosakulrat, C., Pakawatpanurut, P., Sinitskii, A., May, S.J., and Gogotsi, Y. (2019). Effects of Synthesis and Processing on Optoelectronic Properties of Titanium Carbonitride MXene. Chem. Mater. *31*, 2941–2951.
10. Matthews, K., Zhang, T., Shuck, C.E., VahidMohammadi, A., and Gogotsi, Y. (2022). Guidelines for Synthesis and Processing of Chemically Stable Two-Dimensional V_2CT_x MXene. Chem. Mater. *34*, 499–509.
11. Wu, M., He, Y., Wang, L., Xia, Q., and Zhou, A. (2020). Synthesis and electrochemical properties of V_2C MXene by etching in opened/closed environments. J. Adv. Ceram. *9*, 749–758.
12. Ghidiu, M., Naguib, M., Shi, C., Mashtalir, O., Pan, L.M., Zhang, B., Yang, J., Gogotsi, Y., Billinge, S.J.L., and Barsoum, M.W. (2014). Synthesis and characterization of two-dimensional Nb_4C_3 (MXene). Chem. Commun. *50*, 9517–9520.
13. Lipatov, A., Alhabeb, M., Lu, H., Zhao, S., Loes, M.J., Vorobeva, N.S., Dall'Agnese, Y., Gao, Y., Gruverman, A., Gogotsi, Y., et al. (2020). Electrical and Elastic Properties of Individual Single-Layer $Nb_4C_3T_x$ MXene Flakes. Advanced Electronic Materials *6*, 1901382.
14. Lipatov, A., Loes, M.J., Vorobeva, N.S., Bagheri, S., Abourahma, J., Chen, H., Hong, X., Gogotsi, Y., and Sinitskii, A. (2021). High Breakdown Current Density in Monolayer $Nb_4C_3T_x$ MXene. ACS Mater. Lett. *3*, 1088–1094.
15. Lin, H., Wang, Y., Gao, S., Chen, Y., and Shi, J. (2018). Theranostic 2D Tantalum Carbide (MXene). Adv. Mater. *30*, 1703284.
16. Nemani, S.K., Zhang, B., Wyatt, B.C., Hood, Z.D., Manna, S., Khaledialidusti, R., Hong, W., Sternberg, M.G., Sankaranarayanan, S.K.R.S., and Anasori, B. (2021). High-Entropy 2D Carbide MXenes: $TiVNbMoC_3$ and $TiVCrMoC_3$. ACS Nano *15*, 12815–12825.
17. Anasori, B., Xie, Y., Beidaghi, M., Lu, J., Hosler, B.C., Hultman, L., Kent, P.R.C., Gogotsi, Y., and Barsoum, M.W. (2015). Two-Dimensional, Ordered, Double Transition Metals Carbides (MXenes). ACS Nano *9*, 9507–9516.
18. Hantanasirisakul, K., Anasori, B., Nemsak, S., Hart, J.L., Wu, J., Yang, Y., Chopdekar, R.V., Shafer, P., May, A.F., Moon, E.J., et al. (2020). Evidence of a magnetic transition in atomically thin $Cr_2TiC_2T_x$ MXene. Nanoscale Horiz. *5*, 1557–1565.
19. Lee, Y., Bae, S., Jang, H., Jang, S., Zhu, S.-E., Sim, S.H., Song, Y.I., Hong, B.H., and Ahn, J.-H. (2010). Wafer-Scale Synthesis and Transfer of Graphene Films. Nano Lett. *10*, 490–493.
20. Kang, K., Xie, S., Huang, L., Han, Y., Huang, P.Y., Mak, K.F., Kim, C.-J., Muller, D., and Park, J. (2015). High-mobility three-atom-thick semiconducting films with wafer-scale homogeneity. Nature *520*, 656–660.
21. Akinola, O., Chakraborty, I., Celio, H., Akinwande, D., and Incorvia, J.A.C. (2021). Synthesis and characterization of Cr_2C MXenes. J. Mater. Res. *36*, 1980–1989.
22. Zou, X., Liu, H., Xu, H., Wu, X., Han, X., Kang, J., and Reddy, K.M. (2021). A simple approach to synthesis Cr_2CT_x MXene for efficient hydrogen evolution reaction. Mater. Today Energy *20*, 100668.
23. Kolubah, P.D., Mohamed, H.O., Ayach, M., Rao Hari, A., Alshareef, H.N., Saikaly, P., Chae, K.-J., and Castaño, P. (2023). W_2N-MXene composite anode catalyst for efficient microbial fuel cells using domestic wastewater. Chem. Eng. J. *461*, 141821.
24. Bagheri, S., Abourahma, J., Lu, H., Vorobeva, N.S., Luo, S., Gruverman, A., and Sinitskii, A. (2023). High-yield fabrication of electromechanical devices based on suspended $Ti_3C_2T_x$ MXene monolayers. Nanoscale *15*, 1248–1259.
25. Lipatov, A., Goad, A., Loes, M.J., Vorobeva, N.S., Abourahma, J., Gogotsi, Y., and Sinitskii, A. (2021). High electrical conductivity and breakdown current density of individual monolayer $Ti_3C_2T_x$ MXene flakes. Matter *4*, 1413–1427.
26. Alhabeb, M., Maleski, K., Anasori, B., Lelyukh, P., Clark, L., Sin, S., and Gogotsi, Y. (2017). Guidelines for Synthesis and Processing of Two-Dimensional Titanium Carbide ($Ti_3C_2T_x$ MXene). Chem. Mater. *29*, 7633–7644.
27. Vorobeva, N.S., Bagheri, S., Torres, A., and Sinitskii, A. (2022). Negative photoresponse in $Ti_3C_2T_x$ MXene monolayers. Nanophotonics *11*, 3953–3960.
28. Shekhirev, M., Busa, J., Shuck, C.E., Torres, A., Bagheri, S., Sinitskii, A., and Gogotsi, Y. (2022). Ultralarge Flakes of $Ti_3C_2T_x$ MXene via Soft Delamination. ACS Nano *16*, 13695–13703.
29. Lipatov, A., Alhabeb, M., Lukatskaya, M.R., Boson, A., Gogotsi, Y., and Sinitskii, A. (2016). Effect of Synthesis on Quality, Electronic Properties and Environmental Stability of Individual Monolayer Ti_3C_2 MXene Flakes. Adv. Electron. Mater. *2*, 1600255.
30. Lipatov, A., Lu, H., Alhabeb, M., Anasori, B., Gruverman, A., Gogotsi, Y., and Sinitskii, A. (2018). Elastic properties of 2D $Ti_3C_2T_x$ MXene monolayers and bilayers. Sci. Adv. *4*, eaat0491.
31. Shuck, C.E., Han, M., Maleski, K., Hantanasirisakul, K., Kim, S.J., Choi, J., Reil, W.E.B., and Gogotsi, Y. (2019). Effect of Ti_3AlC_2 MAX Phase on Structure and Properties of Resultant $Ti_3C_2T_x$ MXene. ACS Appl. Nano Mater. *2*, 3368–3376.
32. Nakamura, K., and Yashima, M. (2008). Crystal structure of NaCl-type transition metal monocarbides MC (M=V, Ti, Nb, Ta, Hf, Zr), a neutron powder diffraction study. Mater. Sci. Eng. B *148*, 69–72.
33. Eremenko, V.N., Velikanova, T.Y., Sleptsov, S.V., and Bondar', A.A. (1990). Phase equilibria during crystallization of alloys in the Cr-Ti-C system. Dopov. Akad. Nauk Ukr. RSR, Ser. A *4*, 74–76.
34. Zhang, Q., Fan, R., Cheng, W., Ji, P., Sheng, J., Liao, Q., Lai, H., Fu, X., Zhang, C., and Li, H. (2022). Synthesis of Large-Area MXenes with High Yields through Power-Focused Delamination Utilizing Vortex Kinetic Energy. Adv. Sci. *9*, e2202748.

Please cite this article in press as: Bagheri et al., Synthesis of high-quality large $Cr_2TiC_2T_x$ MXene monolayers, their mechanical properties, *p*-type electrical transport, and positive photoresponse, MATT (2024), https://doi.org/10.1016/j.matt.2024.08.019

35. Michałowski, P.P., Anayee, M., Mathis, T.S., Kozdra, S., Wójcik, A., Hantanasirisakul, K., Jóźwik, I., Piątkowska, A., Możdżonek, M., Malinowska, A., et al. (2022). Oxycarbide MXenes and MAX phases identification using monoatomic layer-by-layer analysis with ultralow-energy secondary-ion mass spectrometry. Nat. Nanotechnol. *17*, 1192–1197.
36. Sarycheva, A., Shanmugasundaram, M., Krayev, A., and Gogotsi, Y. (2022). Tip-Enhanced Raman Scattering Imaging of Single- to Few-Layer $Ti_3C_2T_x$ MXene. ACS Nano *16*, 6858–6865.
37. Pazniak, H., Plugin, I.A., Loes, M.J., Inerbaev, T.M., Burmistrov, I.N., Gorshenkov, M., Polcak, J., Varezhnikov, A.S., Sommer, M., Kuznetsov, D.V., et al. (2020). Partially Oxidized $Ti_3C_2T_x$ MXenes for Fast and Selective Detection of Organic Vapors at Part-per-Million Concentrations. ACS Appl. Nano Mater. *3*, 3195–3204.
38. Loes, M.J., Bagheri, S., Vorobeva, N.S., Abourahma, J., and Sinitskii, A. (2023). Synergistic Effect of TiS_3 and $Ti_3C_2T_x$ MXene for Temperature-Tunable p-/n-Type Gas Sensing. ACS Appl. Nano Mater. *6*, 9226–9235.
39. Liu, S., Wang, M., Liu, G., Wan, N., Ge, C., Hussain, S., Meng, H., Wang, M., and Qiao, G. (2021). Enhanced NO_2 gas-sensing performance of 2D Ti_3C_2/TiO_2 nanocomposites by in-situ formation of Schottky barrier. Appl. Surf. Sci. *567*, 150747.
40. Lipatov, A., Bagheri, S., and Sinitskii, A. (2024). Metallic Conductivity of $Ti_3C_2T_x$ MXene Confirmed by Temperature-Dependent Electrical Measurements. ACS Mater. Lett. *6*, 298–307.
41. Miranda, A., Halim, J., Barsoum, M.W., and Lorke, A. (2016). Electronic properties of freestanding $Ti_3C_2T_x$ MXene monolayers. Appl. Phys. Lett. *108*, 033102.
42. Barsoum, M.W., and Gogotsi, Y. (2023). Removing roadblocks and opening new opportunities for MXenes. Ceram. Int. *49*, 24112–24122.
43. Xie, Y., and Kent, P.R.C. (2013). Hybrid density functional study of structural and electronic properties of functionalized $Ti_{(n+1)}X_n$ (X = C, N) monolayers. Phys. Rev. B *87*, 235441.
44. Caffrey, N.M. (2018). Effect of mixed surface terminations on the structural and electrochemical properties of two-dimensional $Ti_3C_2T_2$ and V_2CT_2 MXenes multilayers. Nanoscale *10*, 13520–13530.
45. Jing, Z., Feng, X., Qiu, Y., Li, N., Wu, K., Cheng, Y., and Xiao, B. (2023). Screening of 225 Double-Transition-Metal o-MXenes for Superior Thermoelectric Property at Room Temperature from First-Principles Electron and Phonon Calculations. J. Phys. Chem. C *127*, 14125–14136.
46. Zhang, S., Zhou, Y., Liang, X., Wang, Y., Wang, T., Yang, J., and Lv, L. (2022). Tuning the Magnetic Properties of $Cr_2TiC_2T_x$ through Surface Terminations: A Theoretical Study. Nanomaterials *12*, 4364.
47. Lee, C., Wei, X., Kysar, J.W., and Hone, J. (2008). Measurement of the Elastic Properties and Intrinsic Strength of Monolayer Graphene. Science *321*, 385–388.
48. Bertolazzi, S., Brivio, J., and Kis, A. (2011). Stretching and Breaking of Ultrathin MoS_2. ACS Nano *5*, 9703–9709.
49. Fu, Z.H., Zhang, Q.F., Legut, D., Si, C., Germann, T.C., Lookman, T., Du, S.Y., Francisco, J.S., and Zhang, R.F. (2016). Stabilization and strengthening effects of functional groups in two-dimensional titanium carbide. Phys. Rev. B *94*, 104103.
50. Suk, J.W., Piner, R.D., An, J., and Ruoff, R.S. (2010). Mechanical Properties of Monolayer Graphene Oxide. ACS Nano *4*, 6557–6564.
51. Zhang, R., Koutsos, V., and Cheung, R. (2016). Elastic properties of suspended multilayer WSe_2. Appl. Phys. Lett. *108*, 042104.
52. Liu, K., Yan, Q., Chen, M., Fan, W., Sun, Y., Suh, J., Fu, D., Lee, S., Zhou, J., Tongay, S., et al. (2014). Elastic properties of chemical-vapor-deposited monolayer MoS_2, WS_2, and their bilayer heterostructures. Nano Lett. *14*, 5097–5103.
53. Sinitskii, A., Dimiev, A., Kosynkin, D.V., and Tour, J.M. (2010). Graphene Nanoribbon Devices Produced by Oxidative Unzipping of Carbon Nanotubes. ACS Nano *4*, 5405–5413.
54. Lipatov, A., Vorobeva, N.S., Li, T., Gruverman, A., and Sinitskii, A. (2021). Using Light for Better Programming of Ferroelectric Devices: Optoelectronic MoS_2-Pb(Zr,Ti)O_3 Memories with Improved On–Off Ratios. Adv. Electron. Mater. *7*, 2001223.
55. Kresse, G., and Furthmüller, J. (1996). Efficient iterative schemes for *ab initio* total-energy calculations using a plane-wave basis set. Phys. Rev. B *54*, 11169–11186.
56. Kresse, G., and Joubert, D. (1999). From ultrasoft pseudopotentials to the projector augmented-wave method. Phys. Rev. B *59*, 1758–1775.
57. Blöchl, P.E. (1994). Projector augmented-wave method. Phys. Rev. B *50*, 17953–17979.
58. Monkhorst, H.J., and Pack, J.D. (1976). Special Points for Brillouin-Zone Integrations. Phys. Rev. B *13*, 5188–5192.
59. Dudarev, S.L., Botton, G.A., Savrasov, S.Y., Humphreys, C.J., and Sutton, A.P. (1998). Electron-energy-loss spectra and the structural stability of nickel oxide: An LSDA+U study. Phys. Rev. B *57*, 1505–1509.
60. Grimme, S., Antony, J., Ehrlich, S., and Krieg, H. (2010). A consistent and accurate ab initio parametrization of density functional dispersion correction (DFT-D) for the 94 elements H-Pu. J. Chem. Phys. *132*, 154104.